1   **Structural classification of neutralizing antibodies against the SARS-CoV-2 spike**

2   **receptor-binding domain suggests vaccine and therapeutic strategies**

3

4   Christopher O. Barnes[1], Claudia A. Jette[1], Morgan E. Abernathy[1], Kim-Marie A. Dam[1], Shannon

5   R. Esswein[1], Harry B. Gristick[1], Andrey G. Malyutin[2], Naima G. Sharaf[3], Kathryn E. Huey-

6   Tubman[1], Yu E. Lee[1], Davide F. Robbiani[4,6], Michel C. Nussenzweig[4,5], Anthony P. West, Jr.[1],

7   Pamela J. Bjorkman[1*]

8

9   [1]Division of Biology and Biological Engineering, California Institute of Technology, Pasadena,

10   CA, USA.

11   [2]Division of Chemistry and Chemical Engineering, California Institute of Technology, Pasadena,

12   CA, USA.

13   [3]Beckman Institute, California Institute of Technology, Pasadena, CA, USA.

14   [4]Laboratory of Molecular Immunology, The Rockefeller University, New York, NY 10065, USA

15   [5]Howard Hughes Medical Institute

16   [6]Present address: Institute for Research in Biomedicine, Università della Svizzera italiana,

17   Bellinzona, Switzerland

18

19   *Corresponding author: bjorkman@caltech.edu

20

21

22

23   **Abstract**

24   The COVID-19 pandemic presents an urgent health crisis. Human neutralizing antibodies

25   (hNAbs) that target the host ACE2 receptor-binding domain (RBD) of the SARS-CoV-2 spike[1-5]

26   show therapeutic promise and are being evaluated clincally[6-8]. To determine structural

27   correlates of SARS-CoV-2 neutralization, we solved 8 new structures of distinct COVID-19

28   hNAbs[5] in complex with SARS-CoV-2 spike trimer or RBD. Structural comparisons allowed

29   classification into categories: (1) *VH3-53* hNAbs with short CDRH3s that block ACE2 and bind

30   only to "up" RBDs, (2) ACE2-blocking hNAbs that bind both "up" and "down" RBDs and can

31   contact adjacent RBDs, (3) hNAbs that bind outside the ACE2 site and recognize "up" and

32   "down" RBDs, and (4) Previously-described antibodies that do not block ACE2 and bind only

33   "up" RBDs[9]. Class 2 comprised four hNAbs whose epitopes bridged RBDs, including a *VH3-53*

34   hNAb that used a long CDRH3 with a hydrophobic tip to bridge between adjacent "down" RBDs,

35   thereby locking spike into a closed conformation. Epitope/paratope mapping revealed few

36   interactions with host-derived *N*-glycans and minor contributions of antibody somatic

37   hypermutations to epitope contacts. Affinity measurements and mapping of naturally-occurring

38   and in vitro-selected spike mutants in 3D provided insight into the potential for SARS-CoV-2

39   escape from antibodies elicited during infection or delivered therapeutically. These

40   classifications and structural analyses provide rules for assigning current and future human

41   RBD-targeting antibodies into classes, evaluating avidity effects, suggesting combinations for

42   clinical use, and providing insight into immune responses against SARS-CoV-2.

43

44

45   Neutralizing antibodies (NAbs) against SARS-CoV-2 protect against infection in animal

46   models[1,3,4,10,11] and are being evaluated for prophylaxis and as therapeutics in humans[7,8]. These

47   antibodies target the SARS-CoV-2 spike (S) trimer[3,5,10,12-17], a viral glycoprotein that mediates

48   binding to angiotensin-converting enzyme 2 (ACE2) receptor[18,19]. S trimer comprises three

49   copies of an S1 subunit containing the receptor-binding domain (RBD) and three copies of S2,

50   which includes the fusion peptide and transmembrane regions[20,21]. The RBDs of SARS-CoV-2

51   and other coronaviruses exhibit flexibility, such that they bind ACE2 only when they are in an

52   "up" conformation, as compared with the "down" RBD conformation of the closed, prefusion S

53   trimer[20-25].

54

55   Many hNAbs isolated from COVID-19 convalescent donors target the RBD, binding to distinct,

56   sometimes non-overlapping, epitopes[3-5,10,12-14,17]. A subset of these antibodies blocks viral entry

57   by binding to the ACE2-binding site on the RBD[6,11,13,15,26,27]. A family of recurrent ACE2-blocking

58   hNAbs is composed of heavy chains (HCs) encoded by the *VH3-53* or *VH3-66* gene

59   segment[3,12,13,16,17,27-29], a majority of which are known or predicted[15,26,28,30,31] to exhibit a common

60   RBD binding mode resulting from the use of germline-encoded residues within the

61   complementarity-determining regions 1 and 2 (CDRH1 and CDRH2) and a CDRH3 that is

62   shorter than the average length (15 amino acids; IMGT[32] CDR definition) in human antibodies[33].

63   Other SARS-CoV-2 RBD-binding antibodies are encoded by *VH3-30*[5], which have also been

64   isolated from SARS-CoV-infected donors[34], and antibodies with a variety of the other VH gene

65   segments[3,5,10,12-17].

66

67   To classify commonalities and differences among RBD-binding hNAbs isolated from

68   convalescent COVID-19 individuals[5], we solved complexes of hNAbs with stabilized (2P and 6P

69   versions)[35,36] of soluble S trimer and used high-resolution details of the binding orientations of

70   *VH1-2, VH1-46, VH3-30, VH3-53, VH4-34*, and *VH5-51* and hNAbs to elucidate rules for binding

71   by four distinct anti-RBD antibody classes (Supplementary Table 2). The hNAbs chosen for

72   structures are highly potent, achieving 90% neutralization in pseudotype virus assays at

73   concentrations ranging from 22-140 ng/mL[5], thus our structural analyses and classifications

74   directly relate to understanding mechanisms of neutralization and potency differences between

75   hNAbs.

76

77   **Class 1: *VH3-53*/short CDRH3 hNAbs that block ACE2 binding and bind "up" RBDs**

78   We solved Fab and Fab-RBD crystal structures of C102 (Supplementary Table 1), which we

79   compared to our previous cryo-EM structure of S trimer complexed with the related hNAb

80   C105[26] (Extended Data Fig. 1,2). Both C102 and C105 are *VH3-53* hNAbs with short (9 and 12

81   residues) CDRH3s (Extended Data Fig. 1g) that were isolated from the same donor[5]. They

82   share structural similarities with each other and with other *VH3-53*/short CDRH3 hNAb

83   structures solved as complexes with RBDs[12,30,37,38] (Extended Data Fig. 2a). Importantly, the

84   C102-RBD structure resembled the analogous portion of the C105-S structure[26] (Extended Data

85   Fig. 2a). These results establish that Fab-RBD structures can reproduce interactions with RBDs

86   in the context of an S trimer; however, Fab-RBD structures do not reveal the state(s) of the

87   antibody-bound RBD in the complex ("up" versus "down") or the potential inter-protomer

88   contacts by Fabs.

89

90   Since the C105 Fab bound either two or three "up" RBDs on S with no observed interactions

91   with "down" RBDs or with adjacent RBDs[26] (Extended Data Fig. 1f), we used the higher-

92   resolution C102 Fab-RBD structure to deduce a more accurate epitope/paratope than possible

93   using the C105-S cryo-EM structure with flexible "up" RBDs (Extended Data Fig. 1a-e). Buried

94   surface area (BSA) calculations showed that the C102 CDRH3 played a relatively minor role in

95   the paratope: of 1045 Å^2 BSA on the antibody (786 Å^2 on the HC; 259 Å^2 on the light chain; LC),

96   CDRH3 accounted for only 254 Å^2 (Extended Data Fig. 2b). This contrasts with the majority of

97 antibodies in which CDRH3 contributes equally or more to the interface with antigen than the

98 sum of CDRH1 and CDRH2 contributions[39]. The epitopes on RBD for all available *VH3-53*/short

99 CDRH3 hNAbs span the ACE2 binding site[15,26,28,30,31] and show common RBD-binding

100 interactions, represented by the C102 epitope (Extended Data Fig. 1b-e), which buried 1017 Å^2

101 on RBD (Extended Data Fig. 2b). The ACE2-blocking epitope for these hNAbs is sterically

102 occluded in the RBD "down" conformation (Fig. 1b; Extended Data Fig. 1f); therefore, class 1

103 hNAbs can only bind to "up" RBDs, as observed in the C105-S structure[26], and as previously

104 discussed, IgGs in this class could crosslink adjacent RBDs within a single trimer to achieve

105 tighter binding through avidity effects[26].

106

107 **Class 2: hNAbs that overlap with the ACE2 binding site and recognize both "up" and**

108 **"down" RBD conformations**

109 In addition to the recurrent *VH3-53* hNAbs with short CDRH3s, a small subset of potently

110 neutralizing *VH3-53* encoded antibodies utilize longer CDRH3s (>15 residues, IMGT definition[32],

111 Extended Data Fig. 1g)[5,12]. A recent structure of a RBD complexed with a *VH3-53*/long CDRH3

112 hNAb (COVA2-39) revealed a different RBD binding mode[38], thus confirming predictions that

113 binding with a C102-like interaction requires a short CDRH3[26,30]. To further elucidate molecular

114 mechanisms for binding of *VH3-53*/long CDRH3 hNAbs, we solved a 3.2 Å cryo-EM structure of

115 C144 (*VH3-53/VL2-14*; 25-residue CDRH3) bound to a S trimer[36] (Extended Data Fig. 3).

116 Despite the ability of ligand-free stabilized S trimers to adopt "up" RBD conformations[36] and

117 modeling suggesting the C144 binding site would be accessible on "up" RBDs (Fig. 1b), the

118 C144-S structure revealed three C144 Fabs bound to a completely closed S with three "down"

119 RBDs (Fig. 1a). The C144 binding mode differs from class 1 hNAbs, whose binding orientation

120 is incompatible with "down" RBD conformations (Fig. 1b). In addition, the binding orientation

121 observed for C144 differs from the binding described for COVA2-39, whose RBD epitope is

122 predicted to be accessible only on "up" RBDs[38] due to steric hinderances imposed on the LC by

123   the $N343_{RBD}$-associated glycan on the adjacent RBD (Extended Data Fig. 1h). Despite

124   orientation differences, the RBD epitopes of C144, C102 and COVA2-39 overlap with the ACE2

125   binding site, suggesting a neutralization mechanism involving direct competition with ACE2 (Fig.

126   1b). [40]

127

128   An interesting feature of C144 binding is that its long CDRH3 bridges between adjacent "down"

129   RBDs to lock the spike glycoprotein into a closed, prefusion conformation, providing an

130   additional neutralization mechanism in which S cannot open to engage ACE2 (Fig. 1c,d). The

131   formation of C144's quaternary epitope is driven by sandwiching CDRH3 residues $F100_D$ and

132    $W100_E$ into a hydrophobic RBD cavity at the base of an *N*-linked glycan attached to $N343_{RBD}$.

133   The cavity comprises the RBD α1 helix (337-344), α2 helix (364-371), and hydrophobic

134   residues ($F374_{RBD}$ and $W436_{RBD}$) at the edge of the RBD 5-stranded β-sheet (Fig. 1e,f). By

135   contrast to CDRH3s of class 1 *VH3-53*/short CDRH3 hNAbs, C144's CDRH3 contributed to a

136   majority (~60%) of the paratope and buried 330 $Å^2$ surface area on the adjacent RBD (Extended

137   Data Fig. 2b), likely explaining observed escape at residue $L455_{RBD}$ (Fig. 1f) in C144 selection

138   experiments[40]. Despite adjacent hydrophobic residues ($F100_D$ and $W100_E$) likely to be solvent-

139   exposed before antigen binding, C144 IgG showed no evidence of non-specific binding in a

140   polyreactivity assay (Extended Data Fig. 1i).

141

142   Given the unusual binding characteristics of C144, we investigated whether antibodies that

143   showed similar S binding orientations in low-resolution negative-stain EM (nsEM)

144   reconstructions[5] utilize similar neutralization mechanisms. We characterized Fab-S cryo-EM

145   structures (overall resolutions from 3.4-3.8 Å) of potent hNAbs (C002, C104, C119, and C121)

146   predicted to compete with ACE2 binding[5], which varied in their V gene segment usage and

147   CDRH3 lengths (Fig. 2, Extended Data Figs. 3,4; Extended Data Table 1). Fab-S cryo-EM

148   structures of these class 2 hNAbs showed bound RBDs in both "up" or "down" conformations,

149   consistent with observations of similar hNAbs from nsEM[5,12] and single-particle cryo-EM

150   studies[10,34,41]. By contrast, the C144-S structure showed Fabs bound only to "down" RBDs (Fig.

151   1), suggesting that C144 binding requires recognition of the closed S trimer, or that C144 Fab(s)

152   initially bound to "up" RBD(s) could trap the closed (3 RBDs "down") S conformation through

153   CDRH3-mediated interactions between adjacent RBDs.

154

155   To better understand commonalities of class 2 RBD epitopes, we further analyzed two

156   additional potent hNAbs, C002 *(VH3-30/VK1-39*, 17-residue CDRH3, IC_{50}=8.0 ng/mL[5]) and

157   C121 (*VH1-2/VL2-23*, 23-residue CDRH3, IC_{50}=6.7 ng/mL[5]), for which cryo-EM Fab-S

158   structures were solved to 3.4 Å and 3.6 Å, respectively (Fig. 2a,b) using crystal structures of

159   unbound C002 and C121 Fabs for fitting (Supplementary Table 1). The C002 and C121 RBD

160   epitopes are focused on the receptor-binding ridge, overlapping with polar and hydrophobic

161   residues along the flat face of the RBD responsible for ACE2 interactions (Fig. 2c-e). Similar to

162   C144, hNAbs C002 and C121 buried most of the RBD epitope against HC CDR loops, with LC

163   CDR loops engaging the receptor-binding ridge (Fig. 3). Interestingly, Fab-S structures of C002,

164   C121, C119 and C104 revealed a quaternary epitope involving an adjacent RBD (Extended

165   Data Figs. 3,4, 5a-c), albeit distinct from the quaternary binding of C144 (Fig. 1c-e). This

166   C102/C121/C119/C104 type of secondary interaction was only observed when a Fab was

167   bound to a "down" RBD and adjacent to an "up" RBD. The extent of the secondary interactions

168   varied depending on the antibody pose (Extended Data Fig. 5a-c). Bridging interactions

169   between adjacent "up" and "down" RBDs would not allow the two Fabs of a single IgG to bind

170   simultaneously to an S trimer. However, this class of antibodies could support bivalent

171   interactions between two adjacent "down" RBDs (Extended Data Fig. 5h, Extended Data Table

172   1).

173

7

174 Characterization of the highest resolution interface (C002-S structure) showed C002 LC

175 framework regions (FWRs) 1 and 2 interfaced with the RBD residues comprising the 5-stranded

176 β-sheet and α-helix that spans residues 440_{RBD}–444_{RBD} (Fig. 2e), which is typically located near

177 the three-fold axis of a closed S trimer. In addition to contacting neighboring RBDs, inter-

178 protomer engagement with the $N165_{NTD}$-associated glycan in the N-terminal domain (NTD) was

179 observed for the class 2 hNAb BD23[13]. If fully processed, the $N165_{NTD}$ glycan could adopt a

180 conformation that would allow interactions with HC FWR3 and CDRH1 (Fig. 2e). However, in

181 the structures reported here, we did not observe $N165_{RBD}$ glycan density beyond the initial

182 GlcNAc.

183

184 Given differences in class 2 hNAb V gene segments, CDRH3 lengths, and antibody poses, we

185 investigated sequence features that drive conserved interactions. Sequence differences

186 between SARS-CoV-2 and SARS-CoV RBD, including at positions 486_{RBD} and 493_{RBD} (F and Q,

187 respectively, in SARS-CoV-2), in the ACE2 receptor-binding motif (RBM) allowed more

188 favorable ACE2 binding to the SARS-CoV-2 RBD[42]. Analysis of interactions by C144, C002, and

189 C121 revealed common interactions with these residues and also for $E484_{RBD}$ by both antibody

190 HC and LC residues (Fig. 3). In particular, class 2 hNAb interactions with $F486_{RBD}$ mimicked

191 ACE2 interactions, in that $F486_{RBD}$ buries into a hydrophobic pocket typically involving

192 CDRL1/CDRL3 tyrosine residues[43] (Fig. 3d,h,l). Mimicking of the ACE2 $F486_{RBD}$ binding pocket

193 by SARS-CoV-2 hNAbs was observed across different LC V gene segments (Extended Data

194 Table 1), suggesting that there is no restriction in LC V gene segment usage for class 2 hNAbs.

195 Interestingly, a germline-encoded feature described for *VH3-53/*short CDRH3 class 1 hNAbs,

196 the CDRH2 SxxS motif, is also found in other class 2 hNAbs (e.g., C121 and C119) despite

197 different VH gene segment usage. Similar to *VH3-53* hNAbs C144 and COVA2-39, the C121

198 CDRH2 SxxS motif forms a potential hydrogen bond network with residue $E484_{RBD}$ (Fig. 3b,j).

199

200   Overall, these results suggest a convergent mode of recognition by germline-encoded residues

201   across diverse VH/VL gene segments for SARS-CoV-2, which may contribute to low levels of

202   somatic hypermutation observed for these hNAbs (Extended Data Fig. 6, Extended Data Table

203   1).

204

205   **Class 3: hNAbs that bind outside the ACE2 binding site and recognize both "up" and**

206   **"down" RBD conformations**

207   C135 is a potent hNAb that showed binding properties distinct from class 1, class 2, and the

208   cross-reactive SARS-CoV antibody CR3022[5] (which we categorized as a class 4 antibody;

209   Extended Data Table 1). To evaluate the mechanism of C135-mediated neutralization of SARS-

210   CoV-2, we solved the cryo-EM structure of a C135-S complex to 3.5 Å (Fig. 4a, Extended Data

211   Fig. 7), using an unbound C135 crystal structure for fitting (Supplementary Table 1). The

212   structure revealed three C135 Fabs bound to an S trimer with 2 "down" and 1 "up" RBDs,

213   although the C135-bound "up" RBD conformation was weakly resolved and therefore not

214   modeled. C135 recognizes an glycopeptidic epitope similar to the cross-reactive SARS-CoV

215   hNAb S309[34], focusing on a region of the RBD near the $N343_{RBD}$ glycan and non-overlapping

216   with the ACE2 binding site (Fig. 4b, Extended Data Fig. 7c,d). Despite differences in binding

217   orientations between C135 and S309, targeting of the RBD epitope was mainly V_H-mediated

218   (the BSA of RBD on the C135 HC represented ~480$Å^2$ of ~700 $Å^2$ total BSA) and included

219   interactions with the core fucose moiety of the $N343_{RBD}$ glycan. The smaller C135 footprint

220   relative to S309 (~700 $Å^2$ versus ~1150 $Å^2$ BSA, respectively; Extended Data Fig. 7c,d) focused

221   on interactions with RBD residues $R346_{RBD}$ and $N440_{RBD}$, which are engaged by residues from

222   HC and LC CDR loops (Fig. 4c,d) and are not conserved between SARS-CoV-2 and SARS-CoV

223   RBDs, rationalizing the lack of SARS-CoV cross-reactivity observed for C135[5].

224

225   The discovery of class 3 hNAbs such as C135 and S309 that were raised during SARS-CoV-2

226   or SARS-CoV natural infections, respectively, and bind outside of the ACE2 binding site,

227   provides the potential for additive neutralization effects when combined with hNAbs that block

228   ACE2, while also limiting viral escape[1,40]. A pair of antibodies in human clinical trials that

229   includes REGN10987[8], a hNAb that binds distal to the ACE2 binding site, prevented SARS-

230   CoV-2 viral escape *in vitro*, but did not show synergistic neutralization[6]. Comparison of C135

231   and REGN10987 interactions with S showed similarities in epitopes (interactions focused on

232   residues $R346_{RBD}$ and $N440_{RBD}$; Extended Fig. 7c,f). However, REGN10987 binding would

233   sterically hinder ACE2 interactions, whereas C135 binding does not (Extended Data Fig. 7b,

234   Fig. 4b). Interestingly, a structure of S complexed with C110 (*VH5-51/VK1-5*), isolated from the

235   same donor as the C102 and C105 (class 1) and C119 and C121 (class 2) hNAbs[5], showed a

236   binding pose resembling REGN10987's (Extended Data Fig. 7b,e-f). The C110 epitope showed

237   similarities with both class 3 and class 2 hNAbs, binding distal to the ACE2 binding motif, but

238   like REGN10987, could potentially sterically interfere with ACE2 (Extended Fig. 7). For each of

239   these class 3 hNAbs, the Fab binding pose suggests that intra-protomer crosslinking by a single

240   IgG is not possible (Extended Data Table 1).

241

242   Class 3 hNAbs add to the anti-SARS-CoV-2 antibody repertoire and could likely be effectively

243   used in therapeutic combinations with class 1 or class 2 hNAbs. However, when using

244   structures to predict whether hNAbs have overlapping epitopes, it is sometimes not sufficient to

245   only examine Fab-RBD structures or even static images of S trimer because of the dynamic

246   nature of the spike. Thus what might appear to be non-overlapping epitopes on an isolated RBD

247   could overlap in some (Fig, 4e,f), but not all (Extended Data Fig. 8), scenarios on a spike trimer,

248   complicating interpretation of competition experiments using monomeric RBDs and S trimers.

249   The opposite can also be true; i.e., two Fabs that are predicted to be accommodated on a trimer

250   could clash on an RBD monomer (Fig. 4g,h). Finally, adjacent monomers in different

251 orientations could accommodate different antibodies that target overlapping sites (Extended

252 Data Fig. 8).

253

254 **RBD substitutions affect hNAb binding to varying extents**

255 VSV reporter viruses pseudotyped with SARS-CoV-2 S can escape by mutation from hNAbs

256 C121, C135, or C144[40], three of the antibodies used for the structural studies reported here.

257 RBD mutations that were selected in response to antibody pressure correlated with the epitopes

258 mapped from the structures of their Fabs complexed with S trimer (Fig. 1,2,4).

259

260 To further assess the effects of these and other RBD substitutions, we assayed hNAbs for

261 which we obtained structural information (eight from this study; C105-S complex from ref.[26]) for

262 binding to mutated RBD proteins. The RBD mutants included two that induced escape from the

263 class 3 hNAb C135 (R346S and N440K)[40] (Fig. 4c,d), one found in circulating isolates[44] that

264 conferred partial resistance to C135 (N439K)[40] (Fig. 4d), a circulating variant (A475V) that

265 conferred resistance to class 1 and 2 *VH3-53* hNAbs[44], two that induced escape from C121 or

266 C144 (E484K and Q493R)[40] (Fig. 3), and a circulating variant that conferred partial resistance to

267 C121 (V483A)[40]. Kinetic and equilibrium constants for the original and mutant RBDs were

268 derived from surface plasmon resonance (SPR) binding assays in which RBDs were injected

269 over immobilized IgGs (Extended Data Fig. 9). Loss of binding affinity was consistent with RBD

270 mutations that conferred escape, with hNAbs within each class being similarly affected by the

271 same point mutations, which was not seen when comparing effects of point mutations between

272 hNAb classes. This suggests that antibody pressure that leads to escape from one hNAb class

273 would be unlikely to affect a different class. These results suggest a therapeutic strategy

274 involving hNAbs of different classes for monoclonal NAb treatment of SARS-CoV-2–infected

275 individuals.

276

Conclusions

The Fab-S structures reported here represent a comprehensive structural, biophysical, and bioinformatics analysis of SARS-CoV-2 NAbs (Extended Data Fig. 10), providing critical information for interpreting correlates of protection for clinical use. The structures reveal a wealth of unexpected interactions of hNAbs with the spike trimer, including five antibodies that reach between adjacent RBDs on the protomers of a single spike trimer. A dramatic example of bridging between spike protomers involved a hNAb, C144, that uses a long CDRH3 with a hydrophobic tip to reach across to an adjacent RBD, resulting in all three RBDs on spike trimer being locked into a closed conformation. This example, and the four other hNAbs that contact adjacent RBDs, demonstrates that crystal structures of Fab-monomeric RBD complexes, while informative for defining a primary epitope on one RBD, do not reveal how antibodies actually recognize the flexible "up"/"down" RBD conformations on the spike trimer that are targeted for neutralization on the virus. Indeed, our cryo-EM structures of Fab-spike trimer complexes showed many possible combinations of recognized RBDs: three "up," two "up" and one "down," one "up" and two "down," and three "down," with some structures showing three Fabs bound per trimer and others showing two Fabs bound per trimer. By analyzing the approach angles of antibodies bound to RBDs on spike trimers, we can predict whether a particular IgG can bind to a single spike trimer to gain potency through avidity effects, which would also render the antibody more resistant to spike mutations. In addition, structural information allowed us to assess RBD mutants that arose in circulating viral isolates and/or were obtained by *in vitro* selection. Taken together, this comprehensive study provides a blueprint for designing antibody cocktails for therapeutics and potential spike-based immunogens for vaccines.

300 **Methods**

301 **Protein Expression**

302 Expression and purification of SARS-CoV-2 ectodomains were conducted as previously

303 described[26]. Briefly, constructs encoded the SARS-CoV-2 S ectodomain (residues 16-1206 of

304 the early SARS-CoV-2 GenBank MN985325.1 sequence isolate with 2P[35] or 6P[36] stabilizing

305 mutations, a mutated furin cleavage site between S1 and S2, a C-terminal TEV site, foldon

306 trimerization motif, octa-His tag, and AviTag) were used to express soluble SARS-CoV-2 S

307 ectodomains. Constructs encoding the SARS-CoV-2 RBD from GenBank MN985325.1

308 (residues 331-524 with C-terminal octa-His tag and AviTag) and mutant RBDs were made as

309 described[26], SARS-CoV-2 2P S, 6P S, and RBD proteins were purified from the supernatants of

310 transiently-transfected Expi293F cells (Gibco) by nickel affinity and size-exclusion

311 chromatography[26]. Peak fractions were identified by SDS-PAGE, and fractions corresponding to

312 S trimers or monomeric RBDs were pooled and stored at 4°C. Fabs and IgGs were expressed,

313 purified, and stored as described[45,46].

314

315 **X-ray crystallography**

316 Crystallization trials were carried out at room temperature using the sitting drop vapor diffusion

317 method by mixing equal volumes of a Fab or Fab-RBD complex and reservoir using a TTP

318 LabTech Mosquito robot and commercially-available screens (Hampton Research). Crystals

319 were obtained in 0.2 M ammonium sulfate, 20% w/v PEG 3350 (C102 Fab), 0.2 M sodium

320 citrate tribasic, 20% w/v PEG 3350 (C102-RBD), 0.2 M lithium sulfate monohydrate, 20% w/v

321 PEG 3350 (C002 Fab), 0.04 M potassium phosphate, 16% w/v PEG 8000, 20% v/v glycerol

322 (C135 Fab), 0.2 M ammonium citrate pH 5.1, 20% PEG 3350 (C121 Fab), or 0.2 M sodium

323 tartrate dibasic dihydrate pH 7.3, 20 % w/v PEG 3350 (C110 Fab). A C135 Fab crystal was

324 directly looped and cryopreserved in liquid nitrogen. Other crystals were quickly cryoprotected in

325 a mixture of well solution with 20% glycerol and then cryopreserved in liquid nitrogen.

13

326

327   X-ray diffraction data were collected for Fabs and the Fab-RBD complex at the Stanford

328   Synchrotron Radiation Lightsource (SSRL) beamline 12-1 on a Pilatus 6M pixel detector

329   (Dectris) at a wavelength of 1.0 Å. Data from single crystals of C121 Fab and C110 Fab were

330   indexed and integrated in XDS[47] and merged using AIMLESS in *CCP4*[48] (Supplementary Table

331   1). Data from single crystals of C102 Fab, C135 Fab, and C002 fab were indexed and

332   integrated using XDS[47] and merged in Phenix[49]. Diffraction data for C002 Fab were

333   anisotropically truncated and scaled using the UCLA Anisotropy Server[50] prior to merging. Data

334   from a single crystal of C102 Fab-RBD complex were indexed and integrated using XIA2[51]

335   implementing DIALS[52,53] and merged using AIMLESS in *CCP4*[48]. For C110 Fab and C121 Fabs,

336   structures were determined by molecular replacement in PHASER[54] using the coordinates for

337   B38 (PDB 7BZ5) or an inferred germline form of the HIV-1 NAb IOMA[55] inferred germline

338   (unpublished), respectively, after removing CDR loops as a search model. For C002 Fab, C102

339   Fab, C102 Fab-RBD, and C135 Fab, structures were determined by molecular replacement in

340   PHASER[54] using B38 Fab coordinates (PDB 7BZ5) after trimming HC and LC variable domains

341   using Sculptor[56] (and for the C102 Fab-RBD data, also RBD coordinates from PDB 7BZ5) as

342   search models. Coordinates were refined using Phenix[49] and cycles of manual building in Coot[57]

343   (Supplementary Table 1).

344

345   **Cryo-EM Sample Preparation**

346   Purified Fabs were mixed with SARS-CoV-2 S 2P trimer[35] or SARS-CoV-2 S 6P trimer[36] (1.1:1

347   molar ratio Fab per protomer) to a final Fab-S complex concentration of 2-3 mg/mL and

348   incubated on ice for 30 minutes. Immediately before deposition of 3 µL of complex onto a 300

349   mesh, 1.2/1.3 AuUltraFoil grid (Electron Microscopy Sciences) that had been freshly glow-

350   discharged for 1 min at 20 mA using a PELCO easiGLOW (Ted Pella), a 0.5% w/v octyl-

351   maltoside, fluorinated solution (Anatrace) was added to each sample to a final concentration of

352 0.02%. Samples were vitrified in 100% liquid ethane using a Mark IV Vitrobot (Thermo Fisher)

353 after blotting at 22°C and 100% humidity for 3 s with Whatman No. 1 filter paper.

354

355 **Cryo-EM Data Collection and Processing**

356 Single-particle cryo-EM data were collected on a Titan Krios transmission electron microscope

357 (Thermo Fisher) operating at 300 kV for all Fab-S complexes except for C144-S, which was

358 collected on a Talos Arctica (Thermo Fisher) operating at 200 kV. Movies were collected using

359 SerialEM automated data collection software[58] with beam-image shift over a 3 by 3 pattern of

360 1.2 μm holes with 1 exposure per hole. Movies were recorded in super-resolution mode on a K3

361 camera (Gatan) for the C144-S dataset on the Arctica (0.435 Å/pixel) or on a K3 behind

362 BioQuantum energy filter (Gatan) with a 20 eV slit on the Krios (0.418 Å/pixel) for all other

363 datasets. Data collections parameters are summarized in Supplementary Table 2. In general,

364 the data processing workflow described below was performed for all data sets in cryoSPARC

365 v2.15[59].

366

367 Cryo-EM movies were patch motion corrected for beam-induced motion including dose

368 weighting within cryoSPARC[59] after binning super-resolution movies. The non-dose-weighted

369 images were used to estimate CTF parameters using CTFFIND4[60] or with cryoSPARC

370 implementation of the Patch CTF job, and micrographs with power spectra that showed poor

371 CTF fits or signs of crystalline ice were discarded. A subset of images were randomly selected

372 and used for reference-free particle picking using Blob picker in cryoSPARC[59]. Particles were

373 subjected to 2D classification and the best class averages that represented different views were

374 used to generate 3 *ab initio* models. The particles from the best classes were used in another

375 2D classification job, and the best set of unique views was utilized as templates for particle

376 picking on the full set of images. Initial particle stacks were extracted, down-sampled x2, and

377 used in heterogeneous refinement against the 3 *ab initio* volumes generated with the smaller

15

378   dataset (*ab initio* volumes used were interpreted as a Fab-S complex, free Fab or dissociated S

379   protomers, and junk/noise class). Particles assigned to the Fab-S volume were further cleaned

380   via iterative rounds of 2D classification to select class averages that displayed unique views and

381   secondary structural elements. Resulting particle stacks were homogenously refined before

382   being split into 9 individual exposure groups based upon collection holes. Per particle CTF and

383   aberration corrections were performed and the resulting particles further 3D refined. Additional

384   processing details are summarized in Supplementary Table 2.

385

386   Given the known heterogeneity of spike trimers[20,21], homogenously refined particles were used

387   for 3D classification in cryoSPARC[59] (*ab initio* job: k=4 classes, class similarity=0.3). This

388   typically resulted in one or two majority Fab-S complexes, with the other minority populated

389   classes representing junk or unbound S trimer. Particles from the good class(es) were further

390   subjected to 3D classification (*ab initio* job: k=4, class similarity=0.7) to attempt to separate

391   various Fab-S complex states. If multiple states were identified (as observed for C002-S and

392   C121-S complexes), particles were heterogeneously refined, followed by re-extraction without

393   binning (0.836Å/pixel) before homogeneous refinement of individual states. For all other

394   datasets, the majority of particles represented one state that was homogenously refined after re-

395   extraction without binning.

396

397   Particle stacks for individual states were non-uniform refined with C1 symmetry and a dynamic

398   mask. To improve resolution at the Fab-RBD interfaces, volumes were segmented in Chimera[61]

399   and the regions corresponding to the NTD_{S1}/RBD_{S1} domains and Fab V_H-V_L domains were

400   extracted and used to generate a soft mask (5-pixel extension, 10-pixel soft cosine edge). Local

401   refinements with the mask resulted in modest improvements of the Fab-RBD interface, which

402   allowed for fitting and refinement of this region. The particles were then subjected to CTF

403   refinement and aberration correction, followed by a focused, non-uniform refinement with

16

404   polished particles imposing C1 symmetry (except for the C144-S complex where C3 symmetry

405   was utilized). Final overall resolutions were according to the gold-standard FSC[62]. Details of

406   overall resolution and locally-refined resolutions according to the gold-standard FSC[62] can be

407   found in Supplementary Table 2.

408

409   **Cryo-EM Structure Modeling and Refinement**

410   Coordinates for initial complexes were generated by docking individual chains from reference

411   structures into cryo-EM density using UCSF Chimera[63]. The following coordinates were used:

412   SARS-CoV-2 S trimers: PDBs 6VYB and 6XKL, "up" RBD conformations: PDB 7BZ5, unbound

413   C102, C002, C110, C135 Fab structures (this study) (Supplementary Table 1). Initial models

414   were then refined into cryo-EM maps using one round of rigid body refinement followed by real

415   space refinement. Sequence-updated models were built manually in Coot[57] and then refined

416   using iterative rounds of refinement in Coot[57] and Phenix[49]. Glycans were modeled at potential

417   *N*-linked glycosylation sites (PNGSs) in Coot[57] using 'blurred' maps processed with a variety of

418   B-factors[64]. Validation of model coordinates was performed using MolProbity[65] (Supplementary

419   Table 2).

420

421   **Structural Analyses**

422   CDR lengths were calculated based on IMGT definitions[32]. Structure figures were made with

423   PyMOL (Version 1.8.2.1 Schrodinger, LLC) or UCSF ChimeraX[61]. Local resolution maps were

424   calculated using cryoSPARC v 2.15[59]. Buried surface areas were calculated using PDBePISA[66]

425   and a 1.4 Å probe. Potential hydrogen bonds were assigned as interactions that were <4.0Å

426   and with A-D-H angle >90˚. Potential van der Waals interactions between atoms were assigned

427   as interactions that were <4.0Å. Hydrogen bond and van der Waals interaction assignments are

428   tentative due to resolution limitations. RMSD calculations following pairwise Cα alignments were

429 done in PyMOL without rejecting outliers. Criteria for epitope assignments are described in

430 figure legends.

431

432 To evaluate whether intra-spike crosslinking by an IgG binding to a single spike trimer was

433 possible (Extended Data Table 1), we first measured the Cα distance between a pair of

434 residues near the C-termini of adjacent Fab C_H1 domains (residue 222_{HC} on each Fab)

435 (Extended Data Fig. 5h). We compared this distance to the analogous distances in crystal

436 structures of intact IgGs (42 Å, PDB 1HZH; 48 Å, PDB 1IGY; 52 Å, PDB 1IGT). To account for

437 potential influences of crystal packing in these measurements, as well as flexibility in the V_H-

438 V_L/C_H1-C_L elbow bend angle and uncertainties in C_H1-C_L domain placement in Fab-S cryo-EM

439 structures, we set a cut-off of ≤65 Å for this measured distance as possibly allowing for a single

440 IgG to include both Fabs. Entries in the "Potential IgG intra-spike binding" column in Extended

441 Data Table 1 are marked "No" if all of the adjacent Fabs in cryo-EM classes of that structure are

442 separated by >65 Å for this measured distance. Entries in the "Potential IgG intra-spike binding"

443 column in Extended Data Table 1 are marked as "Yes" if at least one pair of the adjacent Fabs

444 in cryo-EM classes of that structure are separated by ≤65 Å for this measured distance.

445

446 **Surface plasmon resonance (SPR) binding experiments**

447 SPR experiments were performed using a Biacore T200 instrument (GE Healthcare). IgGs were

448 immobilized on a CM5 chip by primary amine chemistry (Biacore manual) to a final response

449 level of ~3000 resonance units (RUs). Concentration series of the original SARS-Cov-2 RBD

450 and RBD mutants (six 4-fold dilutions starting from a top concentration of 1000 nM) were

451 injected at a flow rate of at a flow rate of 30 µL/min over immobilized IgGs for a contact time of

452 60 sec, followed by a injection of 0.01 M HEPES pH 7.4, 0.15 M NaCl, 3 mM EDTA, 0.005% v/v

453 surfactant P20 buffer for a dissociation time of 300 sec. Binding reactions were allowed to reach

454 equilibrium, and K_Ds were calculated from the ratio of association and dissociation rates (K_D =

455   k_d/k_a) derived from a 1:1 binding model (C002, C102, C105, C110, and C119 (except for C119-

456   E484K), C121, C135, and C144), or from a two-state binding model ($K_D = k_d1/k_a1 \times$

457   $k_d2/[k_d2+k_a2]$) (C104, C119-E484K). Kinetic constants were calculated using Biacore T200

458   Evaluation Software v3.2 using a global fit to all curves in each data set. Flow cells were

459   regenerated with 10 mM glycine pH 2.0 at a flow rate of 90 µL/min.

460

461   **Polyreactivity assays**

462   IgGs were evaluated for off-target interactions by measuring binding to baculovirus extracts

463   containing non-specific proteins and lipids as described[60]. The assays were automated on a

464   Tecan Evo2 liquid handling robot fitted with a Tecan Infinite M1000 plate reader capable of

465   reading luminescence. Maxisorb 384-well plates (Nunc) were adsorbed overnight with a 1%

466   preparation of recombinant baculovirus particles generated in Sf9 insect cells[67]. The adsorbed

467   plate was blocked with 0.5% BSA in PBS, then incubated with 20 µL of a 1.0 µg/mL solution of

468   IgG in PBS for 3 hours. Polyreactivity was quantified by detecting bound IgG using an HRP-

469   conjugated anti-human IgG secondary antibody (Genscript) and SuperSignal ELISA Femto

470   Maxiumum Sensitivity Substrate (Thermo Scientific). Relative Light Units (RLU) were measured

471   at 475 nm in the integrated plate reader. Engineered human anti-HIV-1 IgGs previously

472   demonstrated to exhibit high levels of polyreactivity (NIH45-46[G54W] and 45-46m2)[61,62] were used

473   as positive controls. NIH45-46, which exhibited intermediate polyreactivity[63], was also evaluated

474   for comparisons. Negative control IgGs with low polyreactivity included the human HIV-1

475   antibodies N6[64] and 3BNC117[63] and bovine serum albumin (BSA). RLU values are presented

476   as the mean and standard deviation of triplicate measurements in Extended Data Fig. 1i.

477

478   **Reporting Summary**

479   Further information on research design is available in the Nature Research Reporting Summary

480   linked to this paper.

481

Data availability

483 The cryo-EM maps and atomic models will be deposited at the EMDB and the PDB. Crystal

484 structure data will be deposited in the PDB. Described materials will be available upon request,

485 in some cases after completion of a materials transfer agreement.

486

Acknowledgements

509   **Author contributions**

510   C.O.B., M.C.N., A.P.W., and P.J.B. conceived the study and analyzed data; D.F.R. and M.C.N.

511   provided monoclonal antibody sequences and plasmids derived from COVID-19 convalescent

512   donors. C.O.B. and K.H.T. performed protein purifications and C.O.B. assembled complexes for

513   cryo-EM and X-ray crystallography studies. C.O.B. performed cryo-EM and interpreted

514   structures with assistance from M.A.E., K.A.D, S.R.E., A.G.M., and N.G.S. C.A.J. and C.O.B.

515   performed and analyzed crystallographic structures, with refinement assistance from M.A.E and

516   K.M.D. Y.E.L. performed polyreactivity assays. H.B.G. performed and analyzed SPR

517   experiments. A.P.W. analyzed antibody sequences. C.O.B., M.C.N., A.P.W., and P.J.B. wrote

518   the paper with contributions from other authors.

519

520

521

522

References

1. Baum, A. et al. REGN-COV2 antibody cocktail prevents and treats SARS-CoV-2 infection in rhesus macaques and hamsters. *bioRxiv* 10.1101/2020.08.02.233320(2020).

2. Baum, A. et al. Antibody cocktail to SARS-CoV-2 spike protein prevents rapid mutational escape seen with individual antibodies. *Science* **369**, 1014-1018 (2020).

3. Rogers, T.F. et al. Rapid isolation of potent SARS-CoV-2 neutralizing antibodies and protection in a small animal model. *Science* 10.1126/science.abc7520(2020).

4. Zost, S.J. et al. Potently neutralizing and protective human antibodies against SARS-CoV-2. *Nature* **584**, 443-449 (2020).

5. Robbiani, D.F. et al. Convergent antibody responses to SARS-CoV-2 in convalescent individuals. *Nature* **584**, 437-442 (2020).

6. Hansen, J. et al. Studies in humanized mice and convalescent humans yield a SARS-CoV-2 antibody cocktail. *Science* 10.1126/science.abd0827(2020). https://clinicaltrials.gov/ct2/show/NCT04452318.

7. ClinicalTrials.gov. A Study of LY3819253 (LY-CoV555) in Preventing SARS-CoV-2 Infection and COVID-19 in Nursing Home Residents and Staff (BLAZE-2). (2020). https://www.nih.gov/news-events/news-releases/clinical-trials-monoclonal-antibodies-prevent-covid-19-now-enrolling.

8. NIH.gov. Clinical trials of monoclonal antibodies to prevent COVID-19 now enrolling. (2020).

9. Yuan, M. et al. A highly conserved cryptic epitope in the receptor-binding domains of SARS-CoV-2 and SARS-CoV. *Science* 10.1126/science.abb7269(2020).

10. Liu, L. et al. Potent neutralizing antibodies against multiple epitopes on SARS-CoV-2 spike. *Nature* 10.1038/s41586-020-2571-7(2020).

11. Kreye, J. et al. A SARS-CoV-2 neutralizing antibody protects from lung pathology in a COVID-19 hamster model. *bioRxiv* 10.1101/2020.08.15.252320(2020).

12. Brouwer, P.J.M. et al. Potent neutralizing antibodies from COVID-19 patients define multiple targets of vulnerability. *Science* **369**, 643-650 (2020).

13. Cao, Y. et al. Potent neutralizing antibodies against SARS-CoV-2 identified by high-throughput single-cell sequencing of convalescent patients' B cells. *Cell* 10.1016/j.cell.2020.05.025(2020).

14. Kreer, C. et al. Longitudinal Isolation of Potent Near-Germline SARS-CoV-2-Neutralizing Antibodies from COVID-19 Patients. *Cell* 10.1016/j.cell.2020.06.044(2020).

15. Shi, R. et al. A human neutralizing antibody targets the receptor-binding site of SARS-CoV-2. *Nature* **584**, 120-124 (2020).

16. Zost, S.J. et al. Rapid isolation and profiling of a diverse panel of human monoclonal antibodies targeting the SARS-CoV-2 spike protein. *Nat Med* 10.1038/s41591-020-0998-x(2020).

17. Seydoux, E. et al. Analysis of a SARS-CoV-2-Infected Individual Reveals Development of Potent Neutralizing Antibodies with Limited Somatic Mutation. *Immunity* **53**, 98-105 e5 (2020).

18. Hoffmann, M. et al. SARS-CoV-2 Cell Entry Depends on ACE2 and TMPRSS2 and Is Blocked by a Clinically Proven Protease Inhibitor. *Cell* **181**, 271-280 e8 (2020).

19. Wang, Q. et al. Structural and Functional Basis of SARS-CoV-2 Entry by Using Human ACE2. *Cell* **181**, 894-904 e9 (2020).

20. Walls, A.C. et al. Structure, Function, and Antigenicity of the SARS-CoV-2 Spike Glycoprotein. *Cell* **181**, 281-292 e6 (2020).

21. Wrapp, D. et al. Cryo-EM structure of the 2019-nCoV spike in the prefusion conformation. *Science* **367**, 1260-1263 (2020).

572   22.   Walls, A.C. et al. Cryo-electron microscopy structure of a coronavirus spike glycoprotein
573   trimer. *Nature* **531**, 114-117 (2016).
574   23.   Yuan, Y. et al. Cryo-EM structures of MERS-CoV and SARS-CoV spike glycoproteins
575   reveal the dynamic receptor binding domains. *Nat Commun* **8**, 15092 (2017).
576   24.   Kirchdoerfer, R.N. et al. Pre-fusion structure of a human coronavirus spike protein.
577   *Nature* **531**, 118-21 (2016).
578   25.   Li, Z. et al. The human coronavirus HCoV-229E S-protein structure and receptor binding.
579   *Elife* **8**(2019).
580   26.   Barnes, C.O. et al. Structures of Human Antibodies Bound to SARS-CoV-2 Spike Reveal
581   Common Epitopes and Recurrent Features of Antibodies. *Cell* **182**, 828-842 e16 (2020).
582   27.   Ju, B. et al. Human neutralizing antibodies elicited by SARS-CoV-2 infection. *Nature*
583   **584**, 115-119 (2020).
584   28.   Wu, Y. et al. A noncompeting pair of human neutralizing antibodies block COVID-19
585   virus binding to its receptor ACE2. *Science* 10.1126/science.abc2241(2020).
586   29.   Chi, X. et al. A potent neutralizing human antibody reveals the N-terminal domain of the
587   Spike protein of SARS-CoV-2 as a site of vulnerability. *bioRxiv*
588   10.1101/2020.05.08.083964(2020).
589   30.   Yuan, M. et al. Structural basis of a shared antibody response to SARS-CoV-2. *Science*
590   10.1126/science.abd2321(2020).
591   31.   Hurlburt, N.K. et al. Structural basis for potent neutralization of SARS-CoV-2 and role of
592   antibody affinity maturation. *bioRxiv* 10.1101/2020.06.12.148692(2020).
593   32.   Lefranc, M.P. et al. IMGT(R), the international ImMunoGeneTics information system(R)
594   25 years on. *Nucleic Acids Res* **43**, D413-22 (2015).
595   33.   Briney, B., Inderbitzin, A., Joyce, C. & Burton, D.R. Commonality despite exceptional
596   diversity in the baseline human antibody repertoire. *Nature* **566**, 393-397 (2019).
597   34.   Pinto, D. et al. Structural and functional analysis of a potent sarbecovirus neutralizing
598   antibody. *Nature* 10.1038/s41586-020-2349-y(2020).
599   35.   Pallesen, J. et al. Immunogenicity and structures of a rationally designed prefusion
600   MERS-CoV spike antigen. *Proc Natl Acad Sci U S A* **114**, E7348-E7357 (2017).
601   36.   Hsieh, C.L. et al. Structure-based Design of Prefusion-stabilized SARS-CoV-2 Spikes.
602   *bioRxiv* 10.1101/2020.05.30.125484(2020).
603   37.   Wu, F. et al. Neutralizing antibody responses to SARS-CoV-2 in a COVID-19 recovered
604   patient cohort and their implications. *medRxiv* 10.1101/2020.03.30.20047365(2020).
605   38.   Wu, N.C. et al. An alternative binding mode of IGHV3-53 antibodies to the SARS-CoV-2
606   receptor binding domain. *bioRxiv* 10.1101/2020.07.26.222232(2020).
607   39.   Marillet, S., Lefranc, M.P., Boudinot, P. & Cazals, F. Novel Structural Parameters of Ig-
608   Ag Complexes Yield a Quantitative Description of Interaction Specificity and Binding
609   Affinity. *Front Immunol* **8**, 34 (2017).
610   40.   Weisblum, Y. et al. Escape from neutralizing antibodies by SARS-CoV-2 spike protein
611   variants. *bioRxiv* 10.1101/2020.07.21.214759(2020).
612   41.   Wang, B. et al. Bivalent binding of a fully human IgG to the SARS-CoV-2 spike proteins
613   reveals mechanisms of potent neutralization. *bioRxiv*
614   10.1101/2020.07.14.203414(2020).
615   42.   Shang, J. et al. Structural basis of receptor recognition by SARS-CoV-2. *Nature*
616   10.1038/s41586-020-2179-y(2020).
617   43.   Yan, R. et al. Structural basis for the recognition of SARS-CoV-2 by full-length human
618   ACE2. *Science* **367**, 1444-1448 (2020).
619   44.   Li, Q. et al. The Impact of Mutations in SARS-CoV-2 Spike on Viral Infectivity and
620   Antigenicity. *Cell* 10.1016/j.cell.2020.07.012(2020).
621   45.   Scharf, L. et al. Broadly Neutralizing Antibody 8ANC195 Recognizes Closed and Open
622   States of HIV-1 Env. *Cell* **162**, 1379-90 (2015).

623   46.   Schoofs, T. et al. Broad and Potent Neutralizing Antibodies Recognize the Silent Face of
624   the HIV Envelope. *Immunity* **50**, 1513-1529 e9 (2019).
625   47.   Kabsch, W. XDS. *Acta Crystallogr D Biol Crystallogr* **66**, 125-32 (2010).
626   48.   Winn, M.D. et al. Overview of the CCP4 suite and current developments. *Acta
627   Crystallogr D Biol Crystallogr* **67**, 235-42 (2011).
628   49.   Adams, P.D. et al. PHENIX: a comprehensive Python-based system for macromolecular
629   structure solution. *Acta Crystallogr D Biol Crystallogr* **66**, 213-21 (2010).
630   50.   Strong, M. et al. Toward the structural genomics of complexes: crystal structure of a
631   PE/PPE protein complex from Mycobacterium tuberculosis. *Proc Natl Acad Sci USA*
632   **103**, 8060-5 (2006).
633   51.   Winter, G. xia2: an expert system for macromolecular crystallography data reduction. *J.
634   Appl. Cryst.* **43**, 186-190 (2010).
635   52.   Bellsten-Edmands, J. et al. Scaling diffraction data in the DIALS software package:
636   algorithms and new approaches for multi-crystal scaling. *Acta Cryst.* **D76**, 385-399
637   (2020).
638   53.   Winter, G. et al. DIALS: implementation and evaluation of a new integration package.
639   *Acta Cryst.* **D74**, 85-97 (2018).
640   54.   McCoy, A.J. et al. Phaser crystallographic software. *J Appl Crystallogr* **40**, 658-674
641   (2007).
642   55.   Gristick, H.B. et al. Natively glycosylated HIV-1 Env structure reveals new mode for
643   antibody recognition of the CD4-binding site. *Nat Struct Mol Biol* **23**, 906-915 (2016).
644   56.   Bunkóczi, G. & Read, R.J. Improvement of molecular-replacement models with Sculptor.
645   *Acta Cryst.* **67**, 303-312 (2011).
646   57.   Emsley, P., Lohkamp, B., Scott, W.G. & Cowtan, K. Features and development of Coot.
647   *Acta Crystallogr D Biol Crystallogr* **66**, 486-501 (2010).
648   58.   Mastronarde, D.N. Automated electron microscope tomography using robust prediction
649   of specimen movements. *J Struct Biol* **152**, 36-51 (2005).
650   59.   Punjani, A., Rubinstein, J.L., Fleet, D.J. & Brubaker, M.A. cryoSPARC: algorithms for
651   rapid unsupervised cryo-EM structure determination. *Nat Methods* **14**, 290-296 (2017).
652   60.   Rohou, A. & Grigorieff, N. CTFFIND4: Fast and accurate defocus estimation from
653   electron micrographs. *J Struct Biol* **192**, 216-21 (2015).
654   61.   Goddard, T.D. et al. UCSF ChimeraX: Meeting modern challenges in visualization and
655   analysis. *Protein Sci* **27**, 14-25 (2018).
656   62.   Bell, J.M., Chen, M., Baldwin, P.R. & Ludtke, S.J. High resolution single particle
657   refinement in EMAN2.1. *Methods* **100**, 25-34 (2016).
658   63.   Goddard, T.D., Huang, C.C. & Ferrin, T.E. Visualizing density maps with UCSF Chimera.
659   *J Struct Biol* **157**, 281-7 (2007).
660   64.   Terwilliger, T.C., Adams, P.D., Afonine, P.V. & Sobolev, O.V. A fully automatic method
661   yielding initial models from high-resolution cryo-electron microscopy maps. *Nat Methods*
662   **15**, 905-908 (2018).
663   65.   Chen, V.B. et al. MolProbity: all-atom structure validation for macromolecular
664   crystallography. *Acta Crystallogr D Biol Crystallogr* **66**, 12-21 (2010).
665   66.   Krissinel, E. & Henrick, K. Inference of macromolecular assemblies from crystalline
666   state. *J Mol Biol* **372**, 774-97 (2007).
667   67.   Davis, M.I., Bennett, M.J., Thomas, L.M. & Bjorkman, P.J. Crystal structure of prostate-
668   specific membrane antigen, a tumor marker and peptidase. *Proc Natl Acad Sci USA*
669   **102**, 5981-6 (2005).
670
671
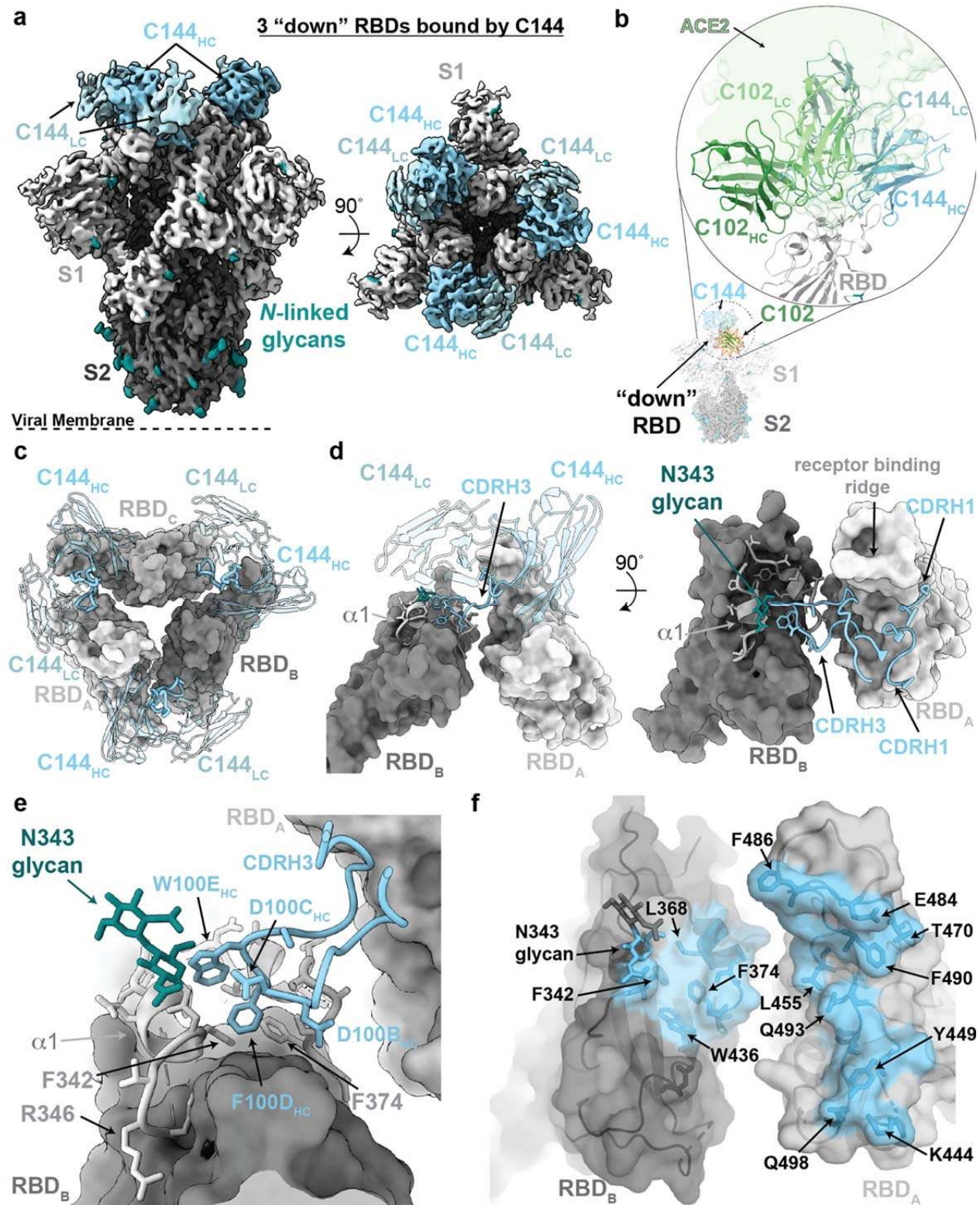
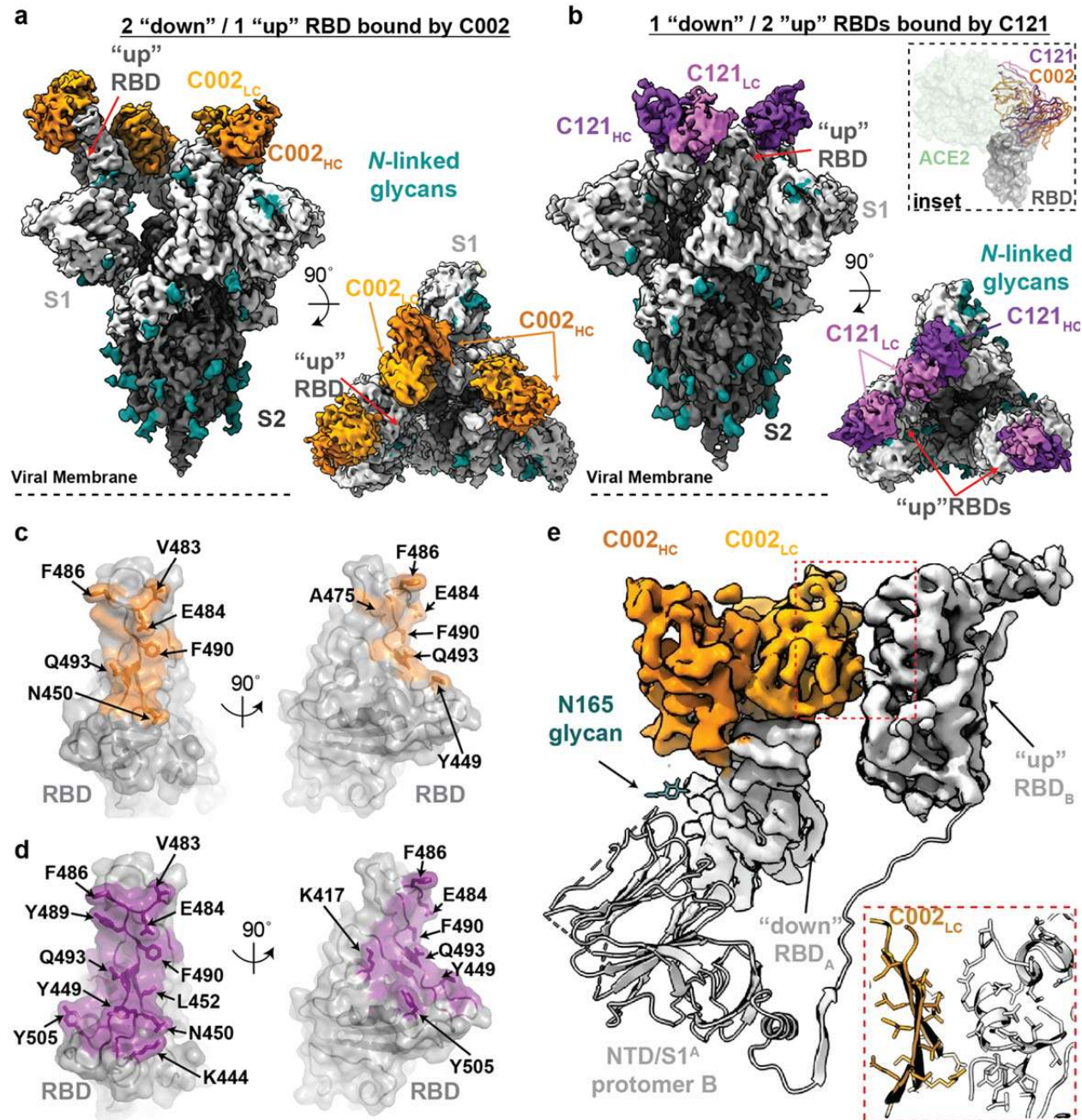**Figure 1**

720   **Figure 1. Cryo-EM structure of the C144-S complex illustrates a distinct *VH3-53* hNAb**

721   **binding mode. a,** 3.2 Å cryo-EM density for C144-S trimer complex revealing C144 binding to a

722   closed (3 RBDs "down") spike conformation. **b,** Overlay of C102 Fab (from C102-RBD crystal

723   structure; Extended Data Fig. 1) and C144 Fab (from C144-S structure) aligned on a RBD

724   monomer. ACE2 (PDB 6M0J; light green surface) is aligned on the same RBD for reference.

725   C144 adopts a distinct conformation relative to the C102-like *VH3-53*/short CDRH3 NAb class,

726   allowing binding to the "down" RBD conformation on trimeric spike, whereas C102-like NAbs

727   can only bind "up" RBDs. **c,** Quaternary epitope of C144 involving bridging between adjacent

728   RBDs via the CDRH3 loop. **d,e,** Close-up view of CDRH3-mediated contacts on adjacent

729   protomer RBD (dark gray). C144 CDRH3 residues $F100_D$ and $W100_E$ are buried in a

730   hydrophobic pocket comprising the RBD α1 helix, residue $F374_{RBD}$ and the $N343_{RBD}$-glycan. **f,**

731   Surface representation of C144 epitope (light blue) across two adjacent RBDs. RBD epitope

732   residues (defined as residues containing atom(s) within 4 Å of a Fab atom) are labeled in black.

733

Figure 2

28

738 **Figure 2. Cryo-EM structures of class 2 C002 and C121 hNAbs show binding to "up" and**

739 **"down" RBDs. a,b**, Cryo-EM densities for C002-S (panel a; 3.4 Å) and C121-S complexes

740 (panel b; 3.7 Å) revealing binding of C002 or C121 to both "down" and "up" RBDs. Inset:

741 Alignment of C002 and C121 Fabs on the same RBD. ACE2 is represented as a green surface

742 for reference. **c,d**, Surface representations of C002 epitope (orange, panel c) and C121 epitope

743 (purple, panel d) on the RBD surface (gray). RBD epitope residues (defined as residues

744 containing atom(s) within 4 Å of a Fab atom) are labeled in black. **e,** C002 forms inter-protomer

745 contacts via binding to an adjacent "up" RBD conformation on the surface of the trimer spike

746 (also observed for class 2 C121-, C119-, and C104-S structures, see Extended Data Fig. 5).

747 Red box: Close-up of adjacent "up" RBD and C002 LC interface.

748

749

750 **Figure 3**
751
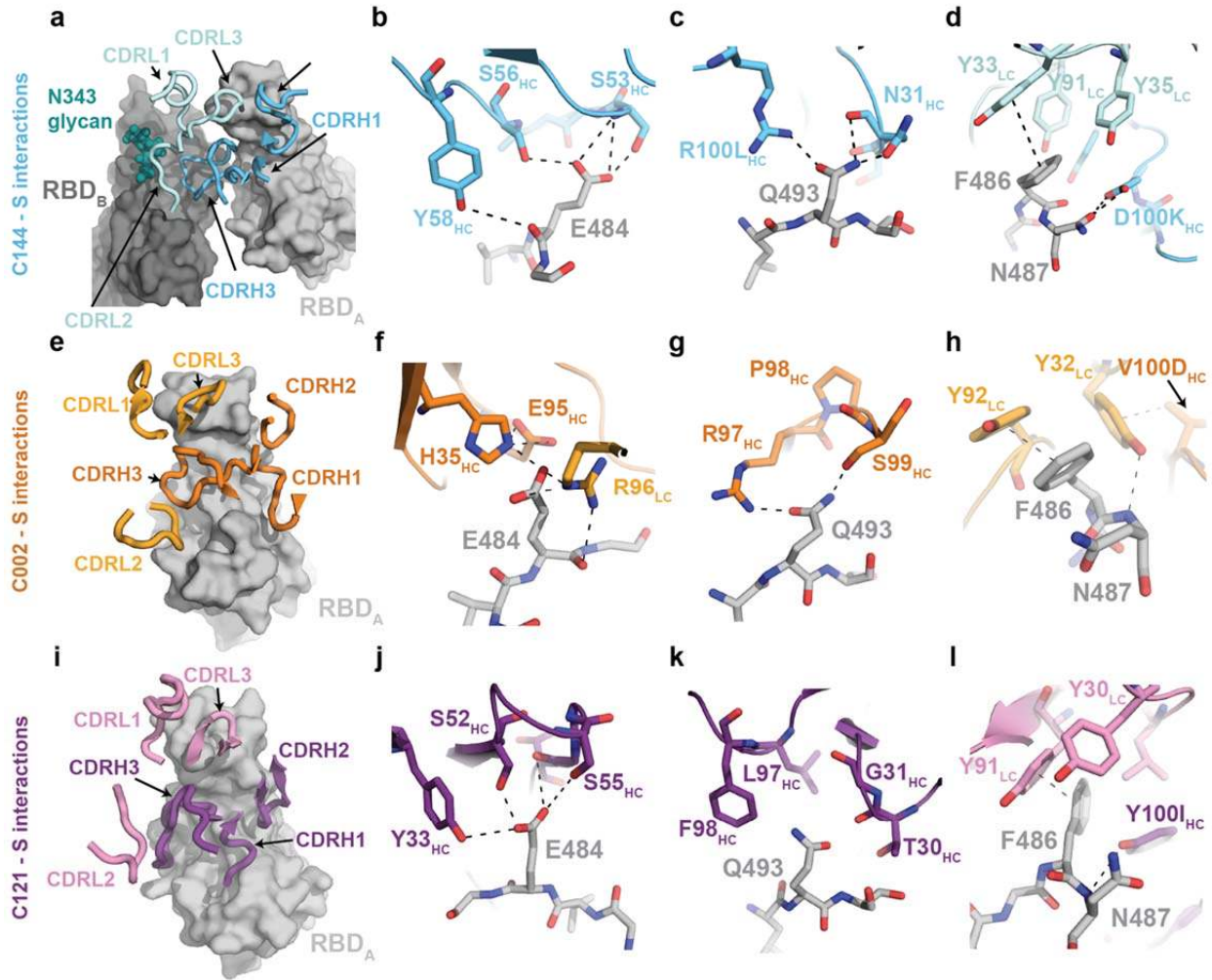
752
753
754
755 **Figure 3. Details of common RBD interactions among class 2 hNAbs.** Conserved

756 interactions between the RBD and CDRs of class 2 NAbs as observed for **a-d,** C144 (HC: cyan,

757 LC: sky blue), **e-h**, C002 (HC: dark orange, LC: light orange), and **i-l**, C121 (HC: purple, LC:

758 pink). Primary and secondary epitopes on adjacent "down" RBDs are shown for C144.

759 Secondary epitopes for C002 and C121, which require adjacent "up" RBDs, are shown in

760 Extended Data Fig. 5. RBDs are gray; potential H-bonds and pi-pi stacking interactions (panel d,

761 $Y33_{LC}$ and $F486_{RBD}$; panel h, $Y92_{LC}$ and $F486_{RBD}$; panel l, $Y91_{LC}$ and $F486_{RBD}$) are indicated by

762 dashed lines.

763

30

764 **Figure 4**
765
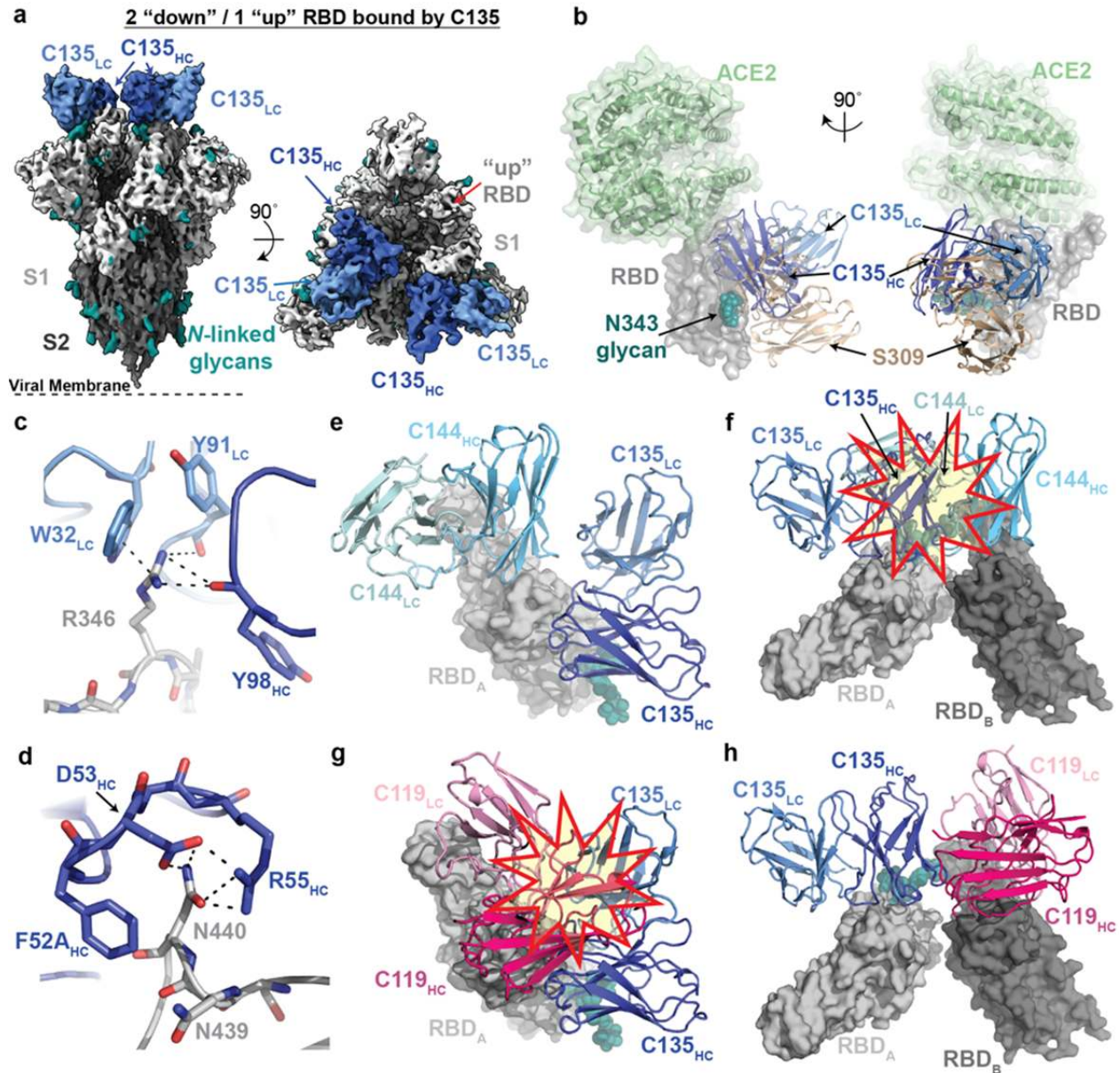
766
767
768 **Figure 4. Cryo-EM structure of S complexed with the class 3 (non-ACE2 blocking) hNAb**

769 **C135. a**, 3.5 Å cryo-EM density of C135-S complex. **b,** Composite model of C135-RBD (blue

770 and gray, respectively) overlaid with the SARS-CoV-2 NAb S309 (sand, PDB 6WPS) and

771 soluble ACE2 (green, PDB 6M0J). The model was generated by aligning on 188 RBD

772 Cα atoms. **c-d,** C135 CDRH (dark blue) and CDRL (light blue) interactions with residues

773 R346$_{RBD}$ (panel c) and N440$_{RBD}$ (panel d). Potential pi-pi stacking interactions in c and H-bonds

31

774   in c and d are illustrated by dashed black lines. **e-f,** Model of RBD interactions of NAbs C135

775   (class 3) and C144 (class 2) demonstrating that both Fabs can bind simultaneously to a single

776   monomeric RBD (panel e), but would clash if bound to adjacent "down" RDBs on S trimer (panel

777   f). Steric clashes indicated by a red and yellow star in f. **g-h,** Model of RBD interaction of NAbs

778   C135 (class 3) and C119 (class 2) demonstrating that both Fabs cannot bind simultaneously to

779   a single monomeric RBD (panel g), but do not clash if bound to adjacent "down" RDBs on S

780   trimer (panel h). Steric clashes indicated by a red and yellow star in g.

781

782

783 **Extended Data Table 1. Anti-SARS-CoV-2 NAb classification and structural properties.**

784

Extended Table 1. Classification and structural properties of SARS-CoV-2 RBD-specific antibodies

Antibody	Reference	IGHV (# of aa SHM)	CDRH3 length (aa)^	IGLV (# of aa SHM)	CDRL3 length (aa)^	IC$_{50}$/IC$_{90}$ (ng/mL)†	Potential IgG intra-spike binding§	Contacts adjacent RBD	Structural Information
Class 1: Blocks ACE2, accessibility of RBD epitope only in "up" conformation									
C102	this study	VH3-53 (2)	11	VK3-20 (0)	9	34 / 143	???	???	3.0 Å Fab-RBD
C105	Barnes, et al.[1]	VH3-53 (0)	12	VL2-8 (1)	11	26.1 / 134	Yes	No	3.4 Å Fab-S. PDB 6XCM
B38	Wu, et al.[2]	VH3-53 (1)	9	VK1-9 (2)	10	117 / NA	???	???	1.8 Å Fab-RBD, PDB 7BZ5
CC12.3	Yuan, et al.[3]	VH3-53 (3)	12	VK3-20 (1)	9	20 / NA	???	???	2.9 Å. Fab-RBD, PDB 6XC7
Class 2: Blocks ACE2, accessibility of RBD epitope in "up"/"down" conformations									
C002	this study	VH3-30 (1)	17	VK1-39 (1)	9	8.9 / 37.6	Yes	Yes	3.4 Å Fab-S
C104	this study	VH4-34 (6)	17	VK3-20 (3)	9	23.3 / 140	Yes	Yes	3.7 Å Fab-S
C119	this study	VH1-46 (1)	20	VL2-14 (3)	11	9.1 / 97.8	Yes	Yes	3.5 Å Fab-S
C121	this study	VH1-2 (2)	22	VL2-23 (0)	10	6.7 / 22.3	Yes	Yes	3.6 Å Fab-S
C144	this study	VH3-53 (3)	25	VL2-14 (1)	10	6.9 / 29.7	Yes	Yes	3.3 Å Fab-S
COVA2-39	Wu, et al.[4]	VH3-53 (3)	17	VL2-23 (1)	10	36 / NA	???	???	1.7 Å Fab-RBD, PDB 7JMP
5A6	Wang, et al.[5]					75.5 / NA	Yes	Yes	2.4 Å Fab-S
P2B-2F6	Ju, et al.[6]	VH4-38*02 (2)	20	VL2-8 (0)	10	50 / NA	???	???	2.9 Å Fab-RBD, PDB 7BWJ
Ab2-4	Liu, et al.[7]	VH1-2 (3)	15	VL2-8 (0)	10	394 / NA	Yes	No	3.2 Å Fab-S, PDB 6XEY
BD23	Cao, et al.[8]	VH7-4*02 (0)	19	VK1-5*03 (0)	9	4800 / NA	No	No	3.8 Å Fab-S, PDB 7BYR
Class 3: Does not overlap with ACE2 binding site, accessibility of RBD epitope in "up"/"down" conformations									
C135	this study	VH3-30 (4)	12	VK1-5 (3)	9	16.6 / 48.9	No	No	3.5 Å Fab-S
S309	Pinto, et al.[9]	VH1-18 (6)	20	VK3-20 (3)	8	79* / NA	No	No	3.1 Å Fab-S, PDB 6WPS
C110	this study	VH5-51 (2)	21	VK1-5 (3)	9	18.4 / 77.3	No	No	3.8 Å Fab-S
REGN10987	Hansen, et al.[10]	VH3-30 (4)	13	VL2-14 (6)	10	6.1 / NA	???	???	3.9 Å Fab-RBD, PDB 6XDG
Class 4: Does not overlap with ACE2 binding site, accessibility of RBD epitope only in "up" conformation									
CR3022	Yuan, et al.[11]	VH5-51 (8)	12	VK4-1 (3)	9	>10,000 / NA	???	???	3.1 Å Fab-RBD, PDB 6W41
COV1-16	Liu, et al.[12]	VH1-46 (1)	20	VK1-33 (3)	10	130 / NA	???	???	2.9 Å Fab-RBD
EY6A	Zhou, et al.[13]	VH3-30*18 (3)	14	VK1-39 (0)	10	70-20,000**/ NA	No	Yes	3.7 Å Fab-S, PDB 6ZDH

^Average human antibody CDRH3 and CDRL3 lengths are 15 (CDRH3) and 9-10 (CDRL3) amino acids.

*IC$_{50}$ calculated against authentic SARS-CoV-2 virus.

**IC$_{50}$ varied depending on neutralization assay utilized.

†Unknown IC$_{90}$s indicated as NA (not available).

§Potential for intra-spike crosslinking by an IgG binding to a single spike trimer was evaluated as described in the Methods.

??? Inference that cannot be made from a structure of a Fab bound to a RBD.

IGHV = Immunoglobulin heavy chain variable gene segment;

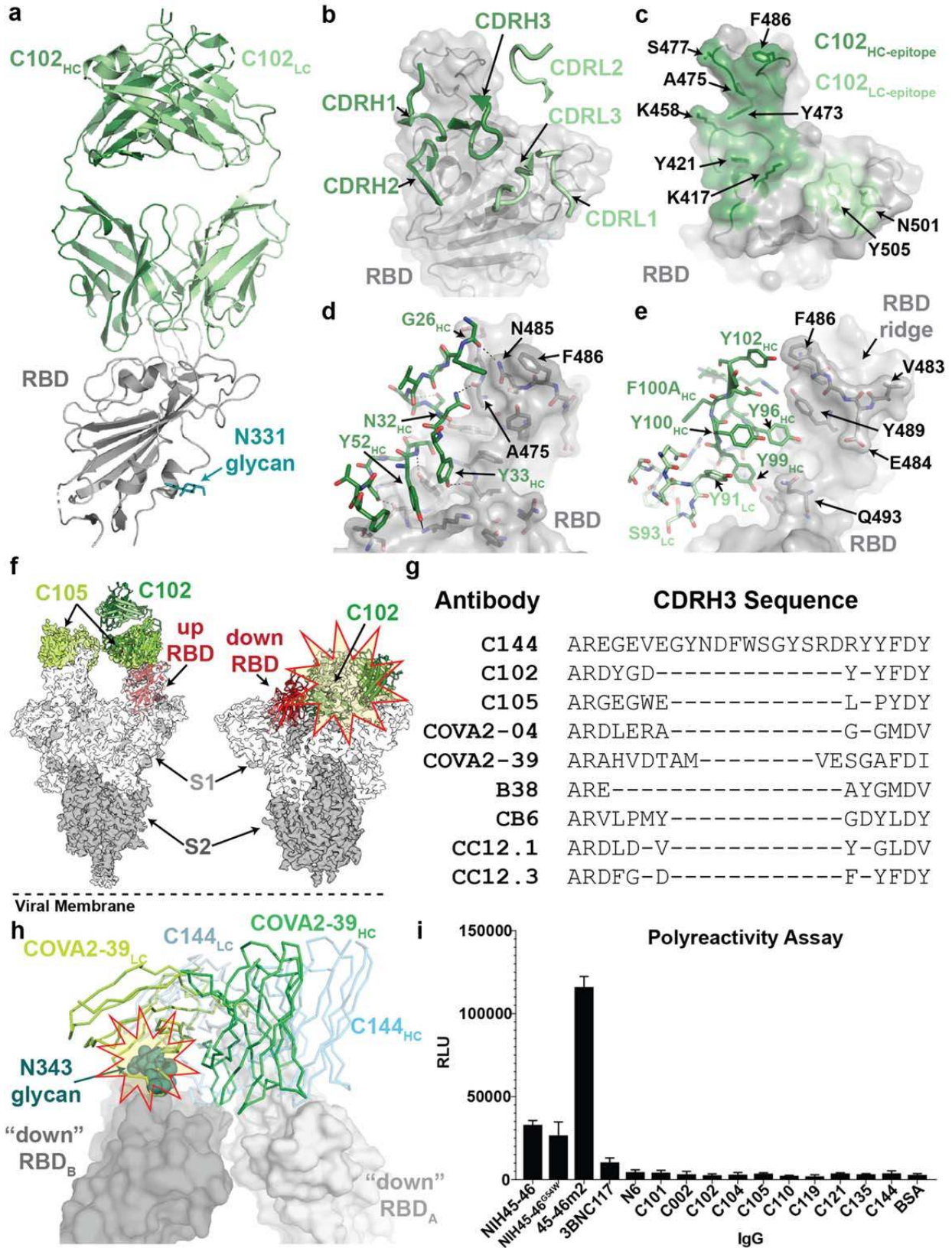IGLV= Immunoglobulin light chain variable gene segment

V gene segments, somatic hypermutation (SHM) information, CDR lengths, IC$_{50}$/IC$_{90}$ values for NAbs in this study are from ref.[14].
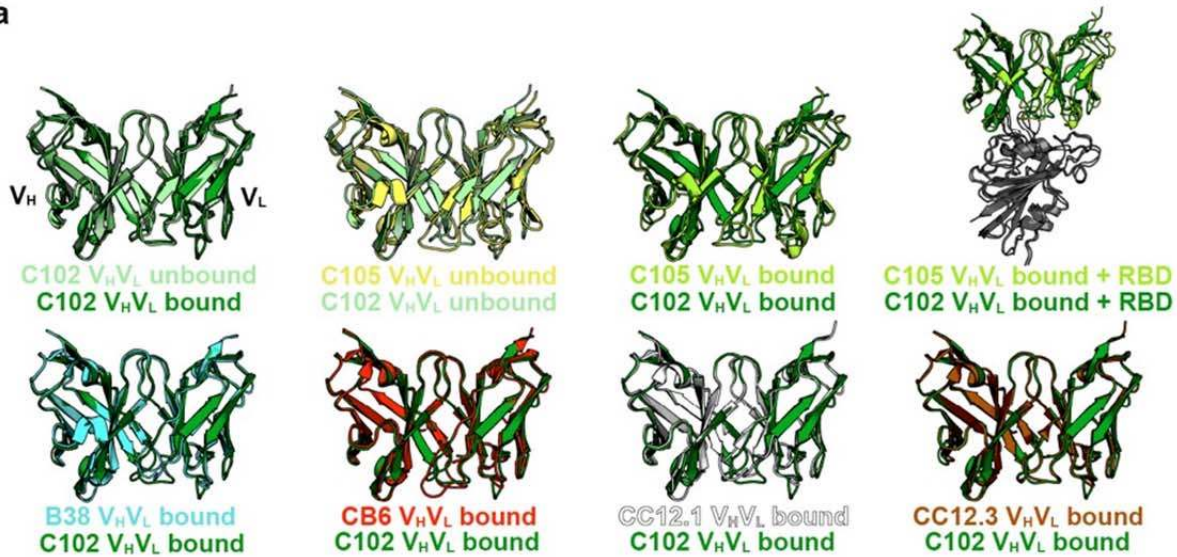
785
786

787 **Extended Data Figure 1**

788

789

790

791 **Extended Data Figure 1: X-ray structure and epitope mapping of *VH3-53* hNAb C102. a,** X-

792 ray structure of C102 Fab – RBD$_{331-518}$ complex. **b,** C102 CDR loops mapped on the RBD

793 surface. **b,** Surface representation of C102 epitope colored by C102 HC (dark green) and LC

794 (light green) interactions. **c,** CDRH1, CDRH2 and **d,** CDRH3 interactions with RBD residues.

795 Potential H-bond contacts are illustrated as dashed lines. **f**, Left: Overlay of C102-RBD crystal

796 structure (cartoon) with C105-S trimer cryoEM density (PDB 6XCM, EMD-22127) illustrating

797 conserved binding to RBD epitope in an "up" conformation. Right: The C102 epitope is sterically

798 occluded when aligned to a "down" RBD conformation (red and yellow star). SARS-CoV-2 S

799 domains are dark gray (S2 domain) and light gray (S1 domain); the C105 Fab is yellow-green.

800 **g,** Alignment of selected CDRH3 sequences for *VH3-53/VH3-66* SARS-CoV-2 neutralizing

801 antibodies (IMGT definition[15]). **h**, Overlay of hNAb COVA2-39 Fab[4] (lime green and lemon, from

802 COVA2-39-RBD structure, PDB 7JMP) and C144 Fab (blue, from C144-S structure) aligned on

803 a RBD$_A$ of C144 epitope. COVA2-39 adopts a distinct conformation relative to the C102-like

804 *VH3-53*/short CDRH3 NAb class and to C144, recognizing its RBD epitope only in an "up" RBD

805 conformations due to steric clashes (red and yellow star) with the N343$_{RBD}$-associated glycan on

806 the adjacent RBD. **i,** Polyreactivity assay. IgGs were evaluated for binding to baculovirus

807 extracts to assess non-specific binding. Polyreactive positive control IgGs were NIH45-46,

808 NIH45-46^{G54W}, and 45-46m2. Negative controls were bovine serum albuminn (BSA) and IgGs

809 N6 and 3BNC117. Relative Light Unit (RLU) values are presented as the mean and standard

810 deviation of triplicate measurements.

811
812
813

814 **Extended Data Figure 2**
815

a

C102 V$_H$V$_L$ unbound / C102 V$_H$V$_L$ bound

C105 V$_H$V$_L$ unbound / C102 V$_H$V$_L$ unbound

C105 V$_H$V$_L$ bound / C102 V$_H$V$_L$ bound

C105 V$_H$V$_L$ bound + RBD / C102 V$_H$V$_L$ bound + RBD

B38 V$_H$V$_L$ bound / C102 V$_H$V$_L$ bound

CB6 V$_H$V$_L$ bound / C102 V$_H$V$_L$ bound

CC12.1 V$_H$V$_L$ bound / C102 V$_H$V$_L$ bound

CC12.3 V$_H$V$_L$ bound / C102 V$_H$V$_L$ bound

Alignments of V$_H$V$_L$ Domains of *VH3-53*/short CDRH3 NAbs

Structure 1	Structure 2	# Ca atoms	RMSD (Å)	PDB Structure 1	PDB Structure 2
C102 unbound	C102 bound	225	0.9	This study	This study
C105 unbound	C102 unbound	220	2.0	6XCA	This study
C105 bound	C102 bound	220	3.0	6XCM	This study
C105 bound + RBD	C102 bound + RBD	403	2.4	6XCM	This study
B38 bound	C102 bound	222	1.1	7BZ5	This study
CB6 bound	C102 bound	223	1.2	7C01	This study
CC12.1 bound	C102 bound	224	1.1	6XC2	This study
CC12.3 bound	C102 bound	224	0.6	6XC4	This study

b

Interface Buried Surface Area (Å^2)							
Structure	C102 Fab/RBD	B38 Fab/RBD	CB6 Fab/RBD	CC12.1 Fab/RBD	CC12.3 Fab/RBD	C144 Fab/RBD	
PDB	this study	7BZ5	7C01	6XC2	6XC4	this study	
VH gene usage	VH3-53/short	VH3-53/short	VH3-53/short	VH3-53/short	VH3-53/short	VH3-53/long	
						RBD A	RBD B
Heavy Chain Paratope	786	736	732	786	721	706	367
FWRH1	150	115	96	107	95	114	0
CDRH1	151	175	133	140	146	52	0
FWRH2	0	0	0	0	0	0	0
CDRH2	230	243	253	255	245	158	0
FWRH3	1	0	0	0	1	64	0
CDRH3	254	203	251	286	233	318	367
FWRH4	0	0	0	0	0	0	0
Light Chain Paratope	259	486	355	560	164	87	20
FWRL1	0	15	0	18	1	0	0
CDRL1	219	239	127	262	111	51	0
FWRL2	0	0	0	0	0	0	0
CDRL2	0	0	0	14	0	0	20
FWRL3	0	35	1	34	0	0	0
CDRL3	40	196	227	231	52	36	0
FWRL4	0	0	0	0	0	0	0
Total Paratope	1046	1222	1087	1347	885	793	387
Heavy Chain Epitope	791	689	736	763	677	722	330
Light Chain Epitope	227	504	313	574	186	100	22
Total Epitope	1017	1193	1049	1337	863	822	351

816

36

817

818 **Extended Data Figure 2. Overview of *VH3-53*/*VH3-66* hNAb structures. a,** Superimposition

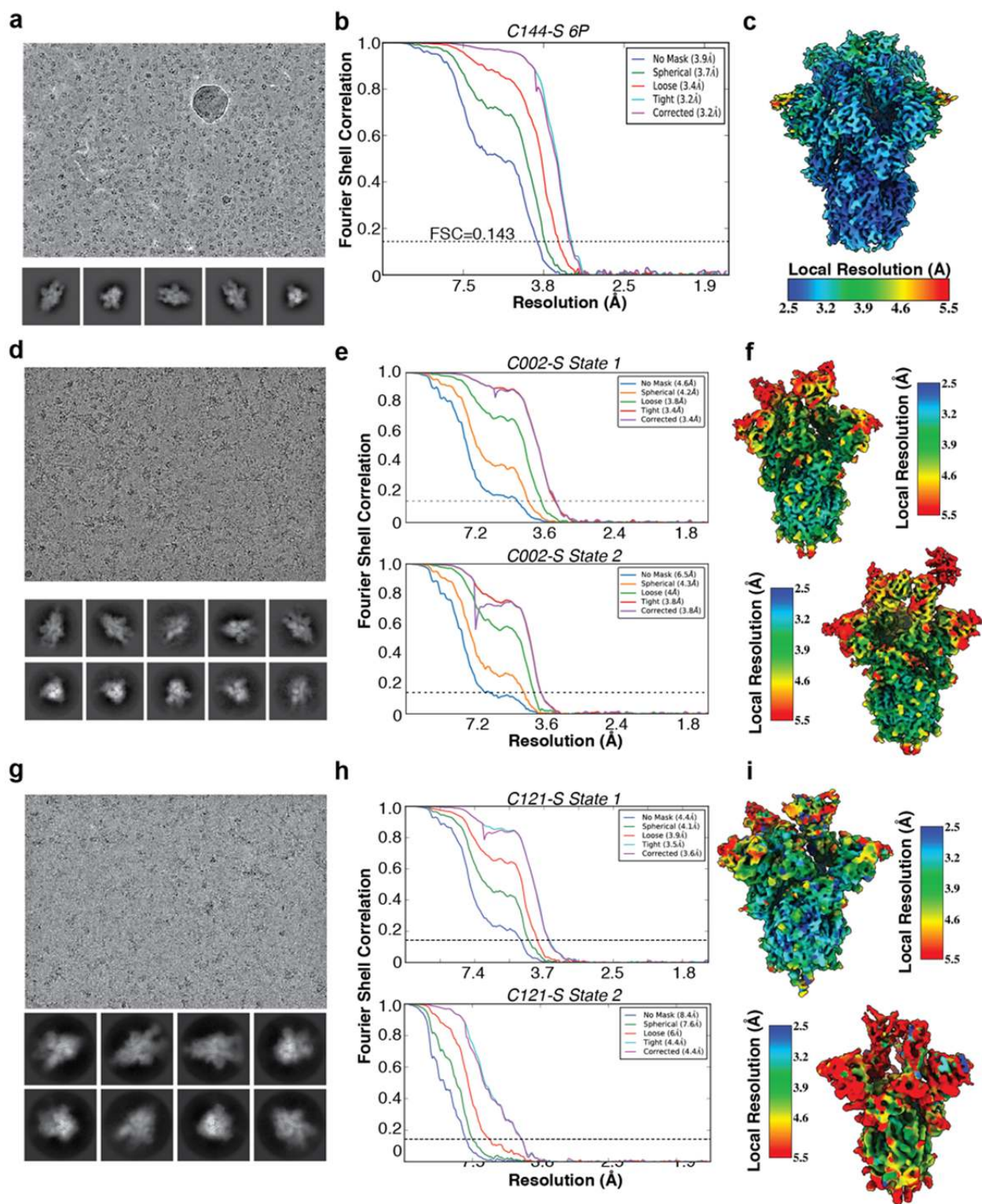819 of V_H and V_L domains of C102 with other *VH3-53*/*VH3-66* NAbs (top) and RMSD calculations

820 (bottom). **b**, BSA comparisons for the indicated Fab/RBD structures. BSAs were calculated

821 using PDBePISA[16] and a 1.4 Å probe.

822
823

824 **Extended Data Figure 3**

825

826
827

828 **Extended Data Figure 3. Cryo-EM data processing and validation for C144-S, C002-S, and**

829 **C121-S complexes.** Representative micrograph, 2D class averages, gold-standard FSC plots,

830 and local resolution estimations for **a-c,** C144-S 6P, **d-f**, C002-S 2P, and **g-l**, C121-S 2P. For

831 the C002-S dataset, two classes were resolved: State 1, C002 Fabs bound to 3 "down" RBDs,

832 and State 2, C002 Fabs bound to 2 "down"/1 "up" RBD. For the C121-S 2P dataset, two classes

833 were resolved: State 1, C121 Fabs bound to 2 "down"/1 "up" RBD and State 2, C121 Fabs

834 bound to 1 "down"/2 "up" RBDs.

835
836
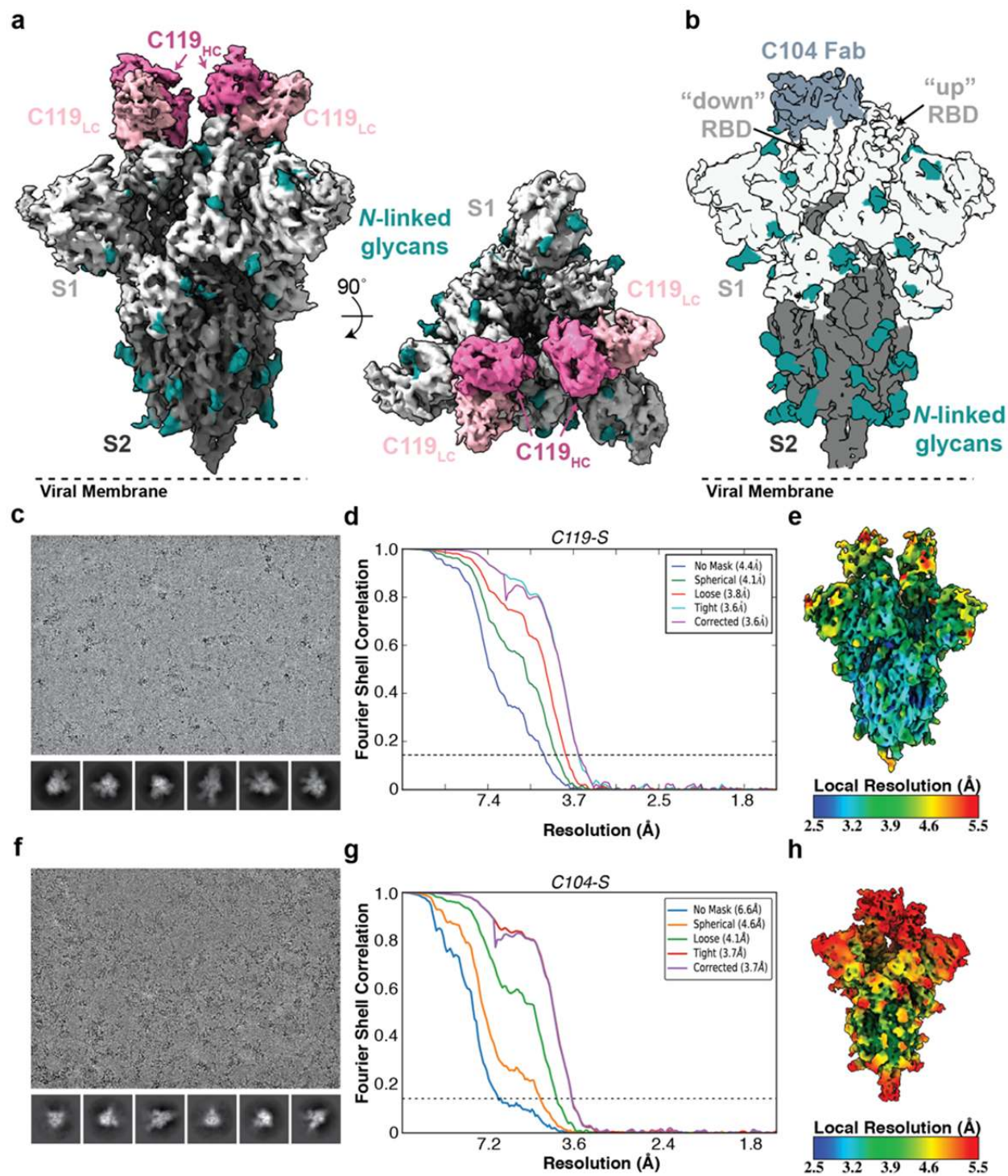
Extended Data Figure 4

Extended Data Figure 4. Cryo-EM processing, validation, and reconstruction for C119-S and C104-S complexes. a, 3.6 Å cryo-EM reconstruction for a C119-S trimer complex. **b,** 3.7 Å

40

843   cryo-EM reconstruction for a C104-S trimer complex. Representative micrograph, 2D class

844   averages, gold-standard FSC plot, and local resolution estimation for **c-e,** C119-S2P and, **d-f,**

845   C104-S. Both complexes revealed binding of Fabs to both "down" and "up" RBD conformations.
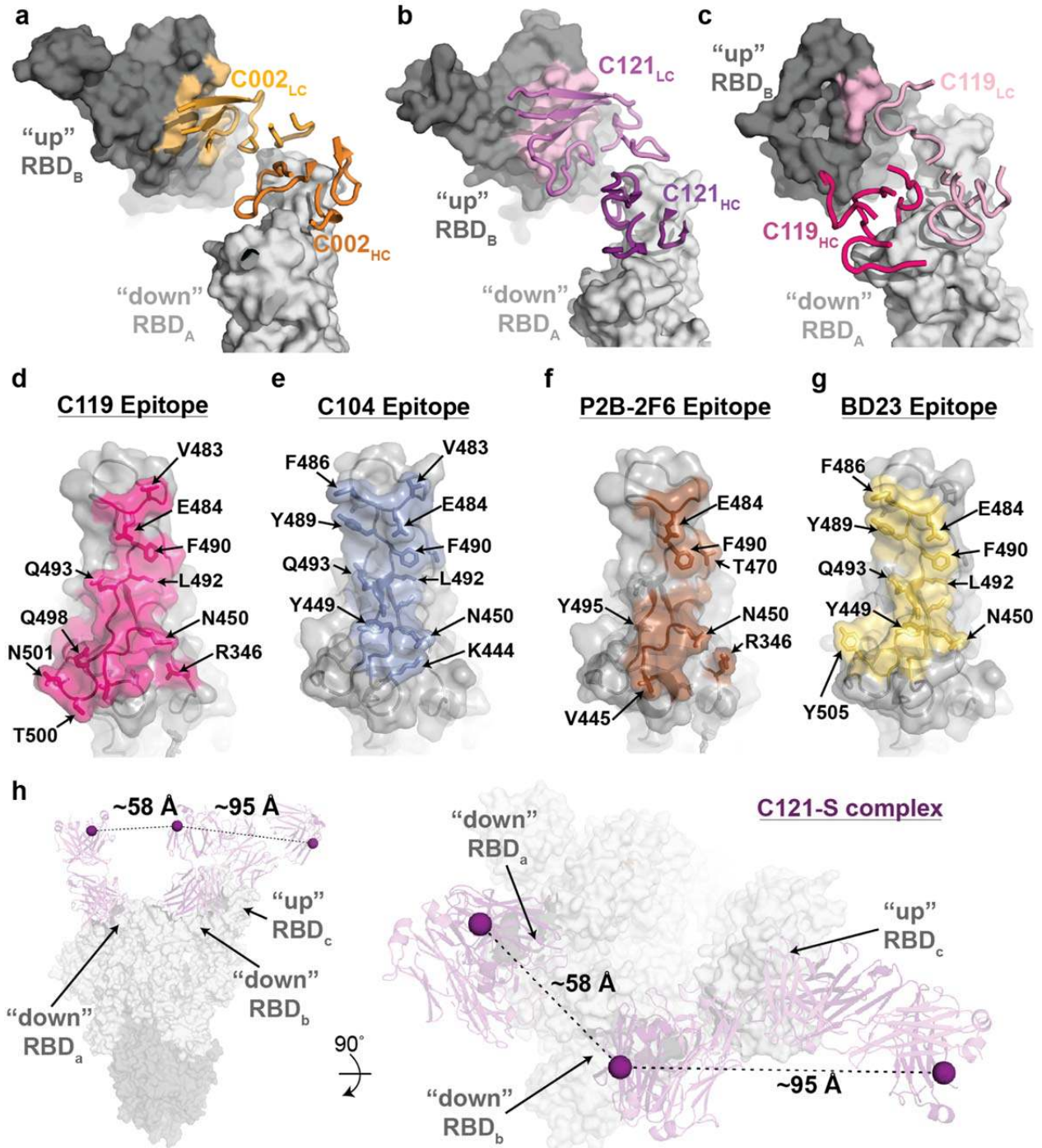
846
847
848
849

Extended Data Figure 5


Extended Data Figure 5. Primary and secondary epitopes of class 2 hNAbs.

a-c, Primary epitopes for C002 (panel a), C121 (panel b), and C119 (panel c) on "down" RBD. A

secondary epitope is observed if a Fab is bound to an adjacent "up" RBD for these NAbs.

42

856   Antibody paratopes are represented as cartoons. A similar interaction in the C104-S structure is

857   not shown due to low local resolution on the "up" RBD. **d-g**, Primary epitopes for C119 (panel

858   d), C104 (panel e), P2B-2F6 (panel f; PDB 7BWJ), and BD23 (panel g, PDB 7BYR). The

859   existence of secondary epitopes for P2B-2F6 and BD23 cannot be determined because the

860   P2B-2F6 epitope was determined from a crystal structure with an RBD[6], and the BD23-S cryo-

861   EM structure showed only one bound Fab[8]. **h**, Measurement of $C\alpha$ distance between the C-

862   termini of adjacent C121 C_H1 domains (residue 222_{HC} on each Fab). Measurements of this type

863   were used to evaluate whether intra-spike crosslinking by an IgG binding to a single spike trimer

864   was possible for hNAbs in Extended Data Table 1.

865

866 **Extended Data Figure 6**

867
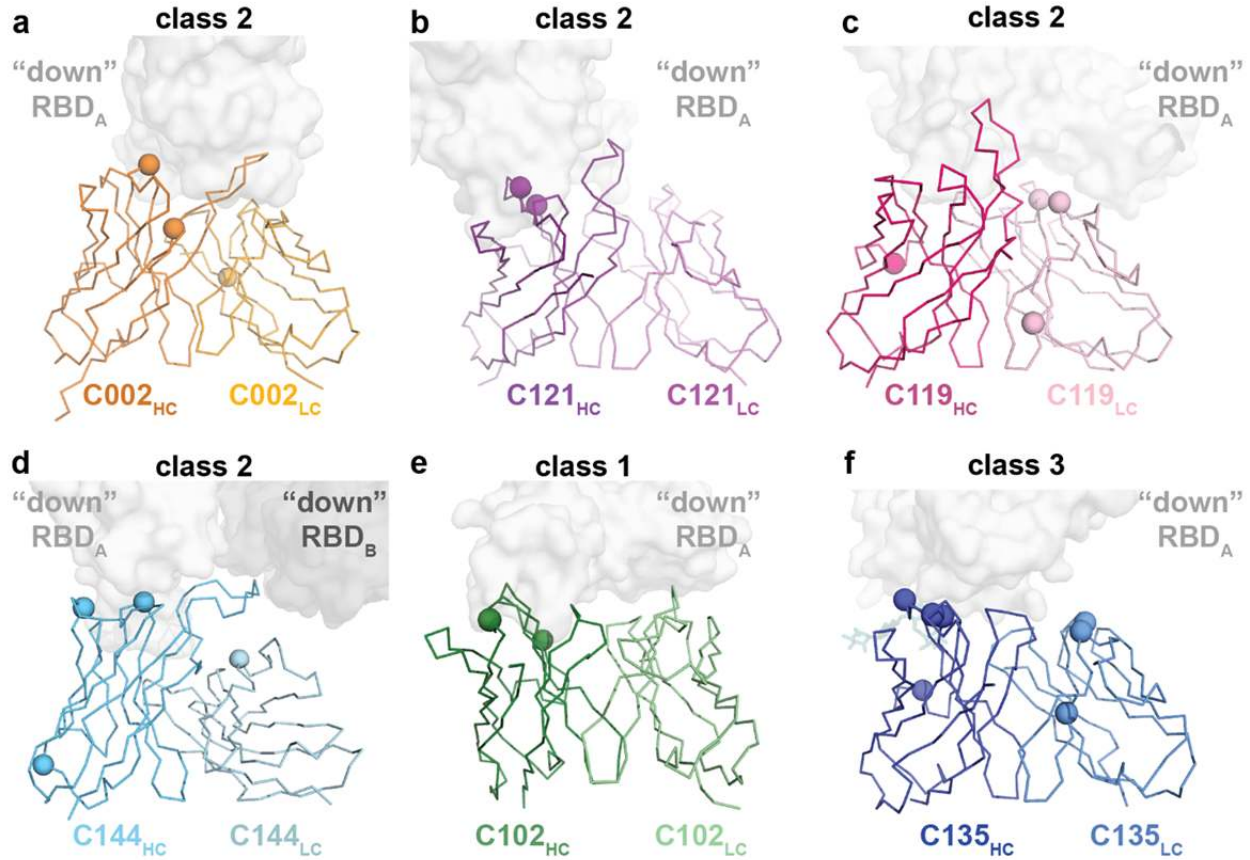
868
869

870 **Extended Data Figure 6. Mapping somatic hypermutations (SHMs) of SARS-CoV-2 NAbs.**

871 **a-f,** Somatic hypermutations in HC and LC V gene segments for C002 (panel a), C121 (panel

872 b), C119 (panel c), C144 (panel d), C102 (panel e) and C135 (panel f) are shown as spheres on

873 the antibody V_H and V_L domains (ribbon representations). The primary RBD epitope is shown as

874 a light gray surface; secondary RBD epitope for C144 is in dark gray.

44

Extended Data Figure 7
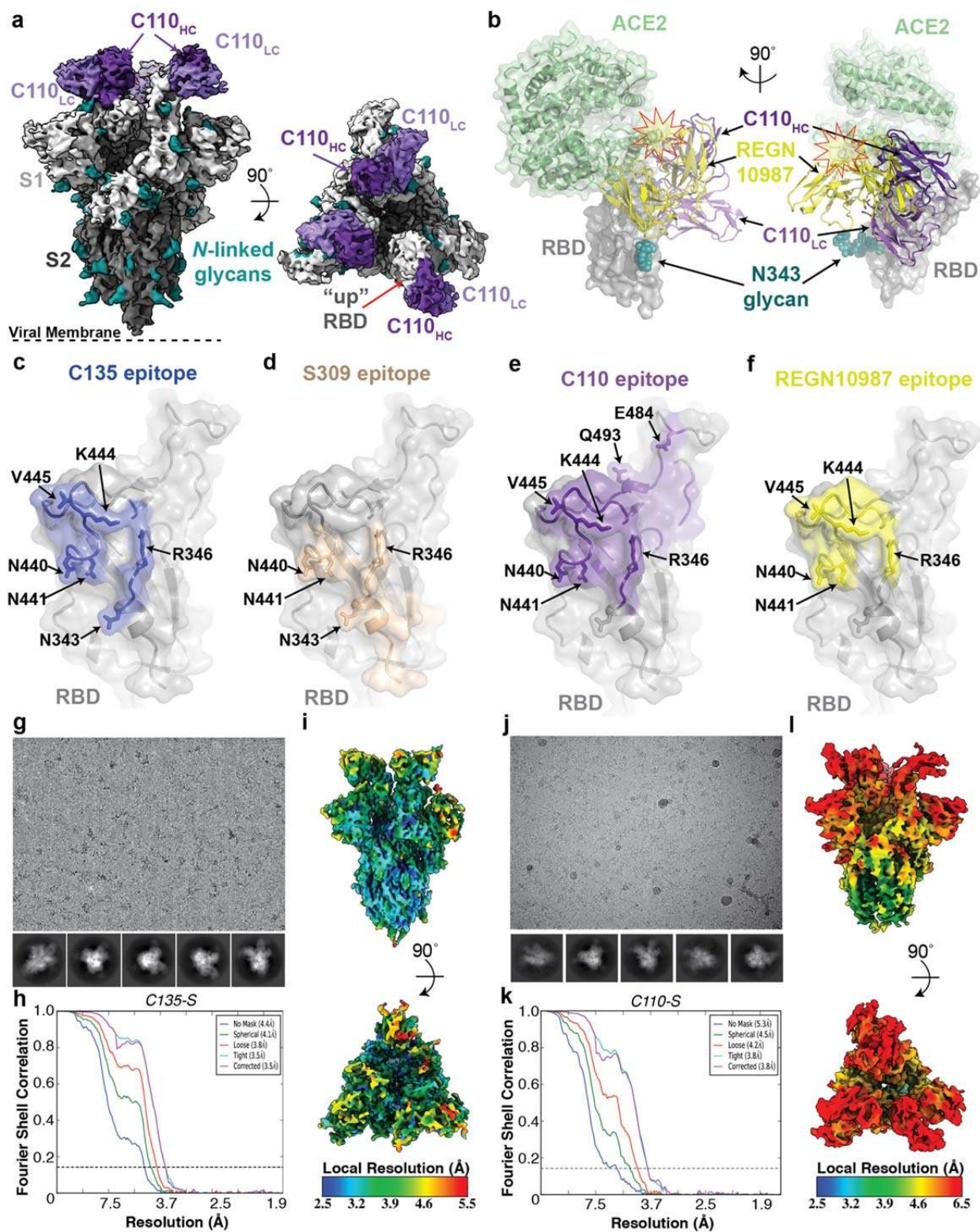
879   **Extended Data Figure 7. Cryo-EM structure of C110-S complex and epitope mapping. a**,

880   3.8 Å cryo-EM reconstruction of C110-S trimer complex. **b,** Composite model of C110-RBD

881   (purple and gray, respectively) overlaid with the SARS-CoV-2 NAb REGN-10987 (yellow, PDB

882   6XDG) and soluble ACE2 (green, PDB 6M0J). Model was generated by aligning structures on

883   188 RBD Cα atoms. **c-f,** Surface representation of RBD epitopes for **c,** C135 (blue), **d,** S309

884   (brown, PDB 6WSP), **e**, C110 (purple) and **f**, REGN-10987 (yellow, PDB 6XDG). Given the low

885   resolution of the antibody-RBD interface, epitopes were assigned by selection of any RBD

886   residue within 7 Å of any antibody Cα atom. Mutation sites found in sequence isolates[17] (green)

887   and in laboratory selection assays[18] (red) are shown. Representative micrograph, 2D class

888   averages, gold-standard FSC plot, and local resolution estimation for **g-i,** C135-S 2P and, **j-l**,

889   C110-S 2P. Both complexes revealed binding of Fabs to both 2 "down"/1 "up" RBD

890   conformations.

891
892

46

893 **Extended Data Figure 8**

894
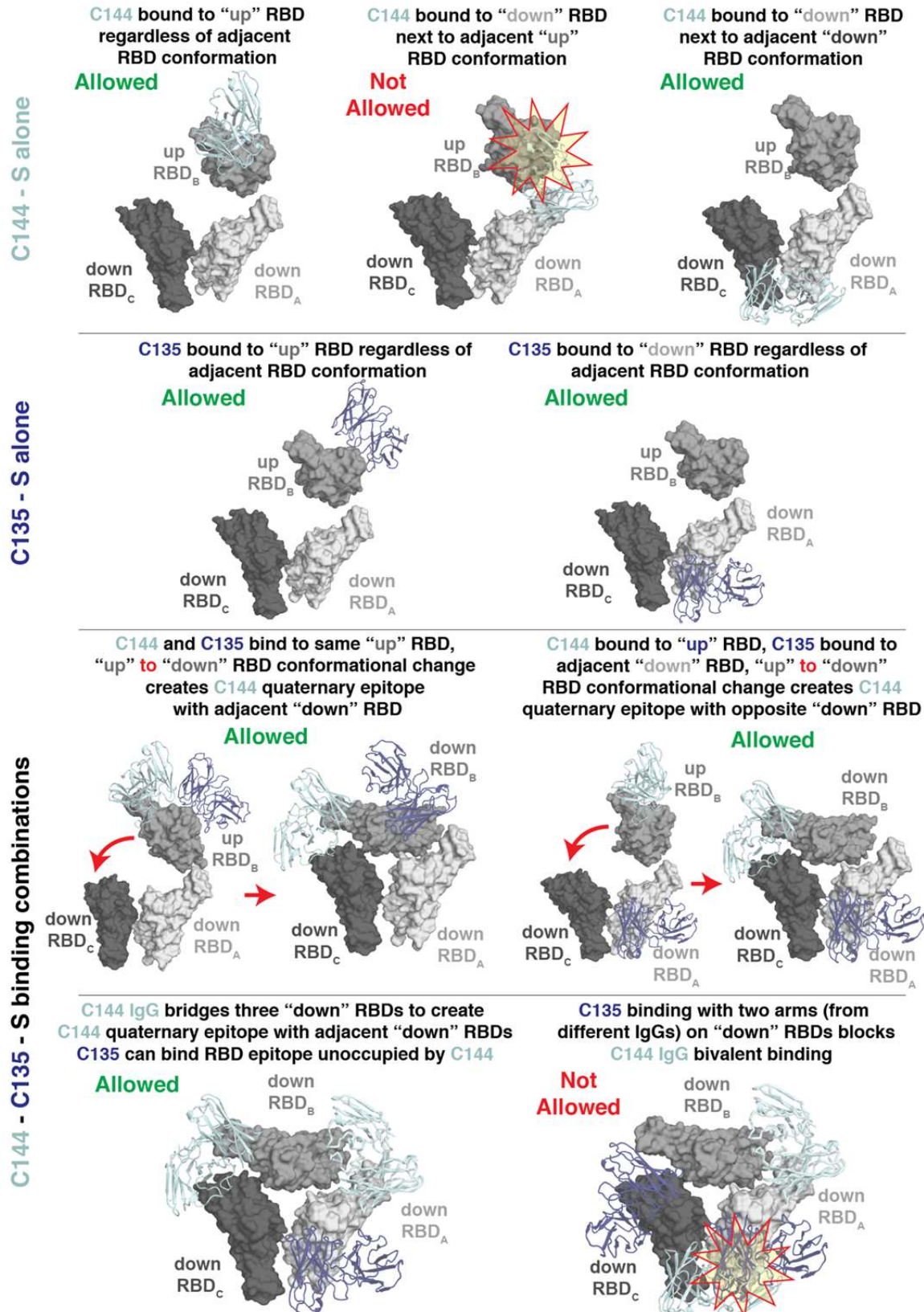
895

896

897 **Extended Data Figure 8. Possibilities for simultaneous engagement of C144 and C135 on**

898 **spikes with different combinations of "up" and "down" RBDs.** Modeling of C144 (light blue)

899 and C135 (dark blue) V_H-V_L domains on different RBD conformations. Steric clashes are shown

900 as a red and yellow star.

901 **Extended Data Figure 9**

902

a

C102
VH3-53/VK3-20 Class 1

RBD	k_a (10^5) ($M^{-1}s^{-1}$)	k_d (10^{-3}) (s^{-1})	K_D (nM)
wt	1.4	3.8	27
R346S	1.2	8.6	72
N439K	1.0	3.2	32
N440K	1.4	7.6	55
A475V	0.8	31.9	395
V483A	1.0	3.1	32
E484K	1.4	8.7	61
Q493R	2.2	17.5	81

C105
VH3-53/VL2-8 Class 1

RBD	k_a (10^5) ($M^{-1}s^{-1}$)	k_d (10^{-3}) (s^{-1})	K_D (nM)
wt	0.7	0.9	14
R346S	0.5	1.1	20
N439K	0.6	1.1	19
N440K	0.6	1.1	18
A475V	1.0	22	225
V483A	0.5	0.8	15
E484K	0.6	1.1	19
Q493R	0.7	0.4	6
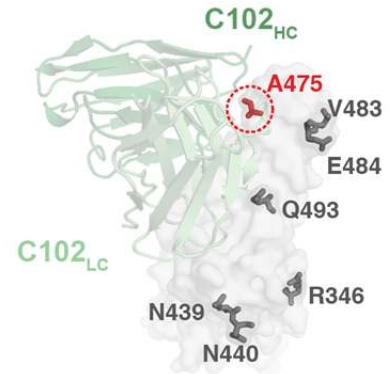
b

C144
VH3-53/VL2-14 Class 2

RBD	k_a (10^5) ($M^{-1}s^{-1}$)	k_d (10^{-3}) (s^{-1})	K_D (nM)
wt	2.3	41.	18
R346S	1.1	5.6	52
N439K	1.2	3.6	29
N440K	1.4	5.8	40
A475V	1070	10820	101
V483A	1.3	4.1	32
E484K	n.b.	n.b.	n.b.
Q493R	n.b.	n.b.	n.b.

C002
VH3-30/VK1-39 Class 2

RBD	k_a (10^5) ($M^{-1}s^{-1}$)	k_d (10^{-3}) (s^{-1})	K_D (nM)
wt	8.3	9.0	11
R346S	3.2	8.6	27
N439K	6.0	9.7	16
N440K	3.3	8.1	24
A475V	2.1	6.3	31
V483A	2.7	2.9	11
E484K	n.b.	n.b.	n.b.
Q493R	1.8	106	596
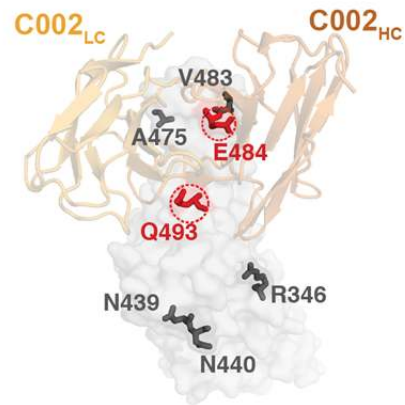
C121
VH1-2/VL2-23 Class 2

RBD	k_a (10^5) ($M^{-1}s^{-1}$)	k_d (10^{-3}) (s^{-1})	K_D (nM)
wt	5.2	2.5	0.5
R346S	6.3	5	0.8
N439K	5.0	3.8	0.8
N440K	6.9	4.1	0.6
A475V	6.4	4.7	0.7
V483A	2.0	1.5	0.8
E484K	n.b.	n.b.	n.b.
Q493R	10	115	111

C119
VH1-46/VL2-14 Class 2

RBD	k_a (10^5) ($M^{-1}s^{-1}$)	k_d (10^{-3}) (s^{-1})	K_D (nM)
wt	2.6	2.6	10
R346S	2.6	5.7	22
N439K	6.4	12.5	20
N440K	1.8	3.8	21
A475V	1.4	2.8	20
V483A	1.7	3.7	22
*E484K	1.1	.005	28	2.7	91
Q493R	5.3	11	20

***C104**
VH4-34/VK3-20 Class 2

RBD	k_a (10^5) ($M^{-1}s^{-1}$)	k_d (10^{-3}) (s^{-1})	K_D (nM)
wt	1.2	.008	17.6	1.3	19
R346S	1.4	.003	28.4	3.3	97
N439K	1.1	.008	28.4	0.9	24
N440K	1.5	.003	31.2	3.7	108
A475V	1.2	.004	25.0	5.2	124
V483A	0.9	.015	24.5	5.4	69
E484K	n.b.	n.b.	n.b.	n.b.	n.b.
Q493R	1.1	.022	36.1	1.2	17

c

C135
VH3-30/VK1-5 Class 3

RBD	k_a (10^5) ($M^{-1}s^{-1}$)	k_d (10^{-3}) (s^{-1})	K_D (nM)
wt	1.9	1.2	6
R346S	n.b.	n.b.	n.b.
N439K	1.3	4.9	37
N440K	n.b.	n.b.	n.b.
A475V	1.5	1.8	12
V483A	1.4	1.3	9
E484K	2.7	1.8	7
Q493R	1.3	1.7	13

C110
VH5-51/VK1-5 Class 3

| RBD	k_a (10^5) ($M^{-1}s^{-1}$)	k_d (10^{-3}) (s^{-1})	K_D (nM)
wt	0.7	0.09	1.3
R346S	0.2	1.1	68
N439K	0.4	0.3	8
N440K	0.5	0.1	2
A475V	0.4	0.1	3
V483A	0.4	0.09	2
E484K	0.4	0.9	27
Q493R	0.3	0.3	12

903

49
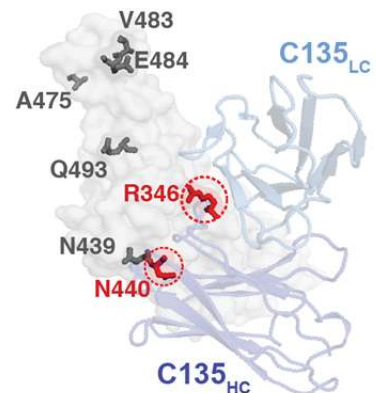
904 **Extended Data Figure 9. SPR binding data for hNAbs.**

905 Kinetic and equilibrium constants for binding to unaltered RBD (indicated as wt) and mutant

906 RBDs are shown in tables beside structures of a representative NAb-RBD complex for each

907 class. Residues that were mutated are highlighted as colored sidechains on a gray RBD

908 surface. Antibody V_H-V_L domains are shown as cartoons. Kinetic and equilibrium constants for

909 NAbs that contact adjacent RBDs on S trimer (C144, C002, C119, and C121) do not account for

910 contacts to a secondary RBD since binding was assayed by injected monomeric RBDs over

911 immobilized IgGs. * indicates kinetic constants determined from a two-state binding model.

912

Extended Data Figure 10
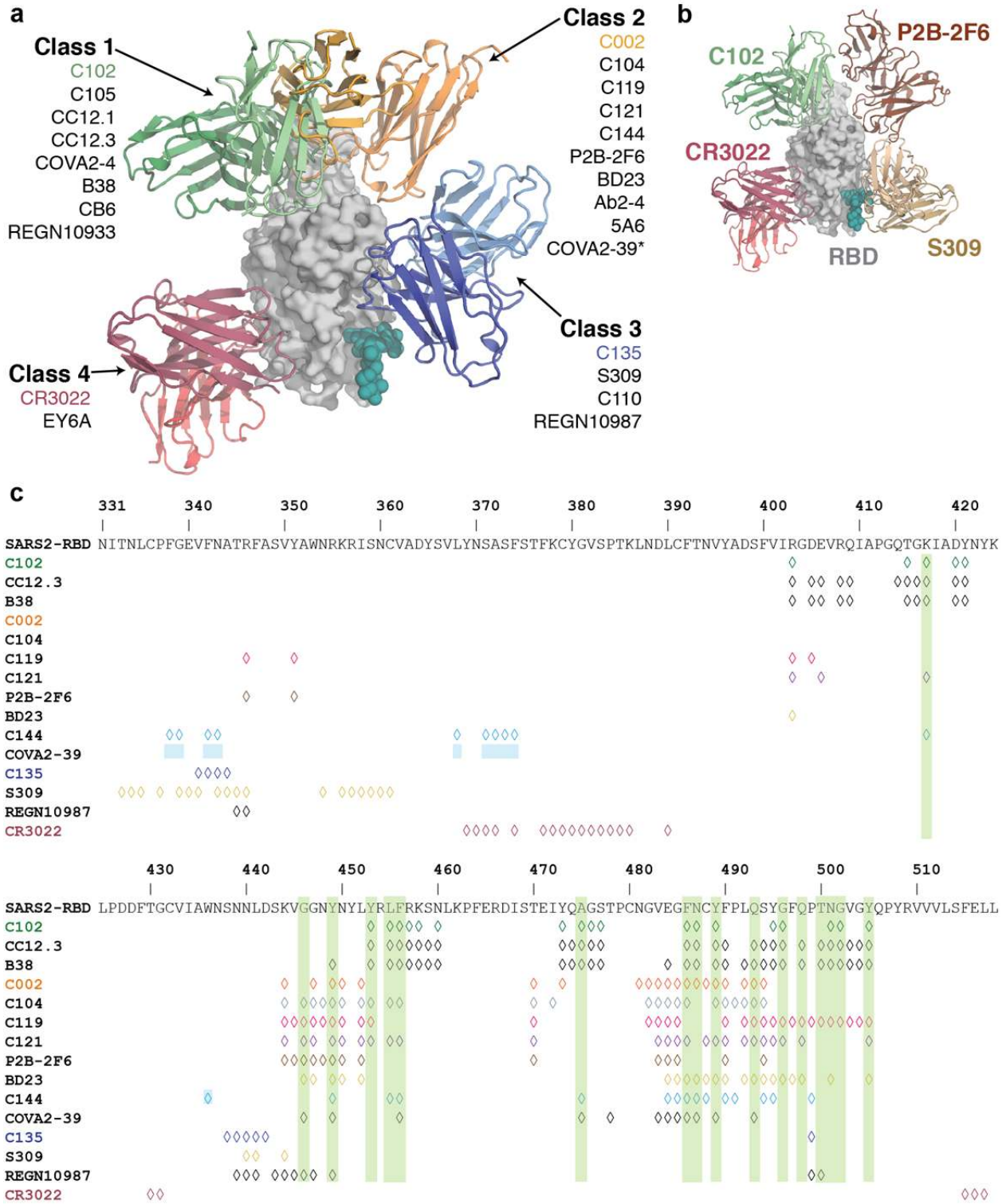
917   **Extended Data Figure 10: Summary of hNAbs. a,** Structural depiction of a representative

918   NAb from each class binding its RBD epitope. **b**, Composite model illustrating non-overlapping

919   epitopes of NAbs from each class bound to a RBD monomer. **c**, Epitopes for SARS-CoV-2

920   NAbs. RBD residues involved in ACE2 binding are boxed in green. Diamonds represent RBD

921   residues contacted by the indicated antibody.

922
923

924

925

Extended Data References

926

927 1. Barnes, C.O. et al. Structures of Human Antibodies Bound to SARS-CoV-2 Spike Reveal
928   Common Epitopes and Recurrent Features of Antibodies. *Cell* **182**, 828-842 e16 (2020).
929 2. Wu, Y. et al. A noncompeting pair of human neutralizing antibodies block COVID-19
930   virus binding to its receptor ACE2. *Science* 10.1126/science.abc2241(2020).
931 3. Yuan, M. et al. Structural basis of a shared antibody response to SARS-CoV-2. *Science*
932   10.1126/science.abd2321(2020).
933 4. Wu, N.C. et al. An alternative binding mode of IGHV3-53 antibodies to the SARS-CoV-2
934   receptor binding domain. *bioRxiv* 10.1101/2020.07.26.222232(2020).
935 5. Wang, B. et al. Bivalent binding of a fully human IgG to the SARS-CoV-2 spike proteins
936   reveals mechanisms of potent neutralization. *bioRxiv*
937   10.1101/2020.07.14.203414(2020).
938 6. Ju, B. et al. Human neutralizing antibodies elicited by SARS-CoV-2 infection. *Nature*
939   **584**, 115-119 (2020).
940 7. Liu, L. et al. Potent neutralizing antibodies against multiple epitopes on SARS-CoV-2
941   spike. *Nature* 10.1038/s41586-020-2571-7(2020).
942 8. Cao, Y. et al. Potent neutralizing antibodies against SARS-CoV-2 identified by high-
943   throughput single-cell sequencing of convalescent patients' B cells. *Cell*
944   10.1016/j.cell.2020.05.025(2020).
945 9. Pinto, D. et al. Structural and functional analysis of a potent sarbecovirus neutralizing
946   antibody. *Nature* 10.1038/s41586-020-2349-y(2020).
947 10. Hansen, J. et al. Studies in humanized mice and convalescent humans yield a SARS-
948   CoV-2 antibody cocktail. *Science* 10.1126/science.abd0827(2020).
949 11. Yuan, M. et al. A highly conserved cryptic epitope in the receptor-binding domains of
950   SARS-CoV-2 and SARS-CoV. *Science* 10.1126/science.abb7269(2020).
951 12. Liu, H. et al. Cross-neutralization of a SARS-CoV-2 antibody to a functionally conserved
952   site is mediated by avidity. *bioRxiv* 10.1101/2020.08.02.233536(2020).
953 13. Zhou, D. et al. Structural basis for the neutralization of SARS-CoV-2 by an antibody from
954   a convalescent patient. *Nat Struct Mol Biol* 10.1038/s41594-020-0480-y(2020).
955 14. Robbiani, D.F. et al. Convergent antibody responses to SARS-CoV-2 in convalescent
956   individuals. *Nature* **584**, 437-442 (2020).
957 15. Lefranc, M.P. et al. IMGT(R), the international ImMunoGeneTics information system(R)
958   25 years on. *Nucleic Acids Res* **43**, D413-22 (2015).
959 16. Krissinel, E. & Henrick, K. Inference of macromolecular assemblies from crystalline
960   state. *J Mol Biol* **372**, 774-97 (2007).
961 17. Li, Q. et al. The Impact of Mutations in SARS-CoV-2 Spike on Viral Infectivity and
962   Antigenicity. *Cell* 10.1016/j.cell.2020.07.012(2020).
963 18. Weisblum, Y. et al. Escape from neutralizing antibodies by SARS-CoV-2 spike protein
964   variants. *bioRxiv* 10.1101/2020.07.21.214759(2020).
965
966